ON-CHIP SPECTROMETER BASED ON PHOTONIC CRYSTAL ZIPPER CAVITY

A thesis presented for the degree of
Master of Science

Faculty of Applied Sciences – Faculteit Technische Natuurwetenschappen
Delft University of Technology –Technische Universiteit Delft
April 2024

by

Hongyi CHEN

Supervisor: Prof. Dr. Simon Gröblacher
Mentor: Mr. Xiong Yao

CONTENTS

SUMMARY

The spectrometers are widely used in various fields ranging from astronomy to biology. Recently, lots of efforts have been made to miniaturize the size of the spectrometer to meet the needs of fields such as real-time health monitoring. Therefore, achieving a high-resolution, broadband on-chip spectrometer is an intriguing but challenging topic. Photonic crystals are constructed by material with periodic refractive indices. They allow us to modify the interaction between electromagnetic fields and dielectric media. In this work, using a special kind of photonic crystal called “zipper cavity”, we design a wavelength tunable filter, which can be used as the key component for a filter-based spectrometer. By FEM simulation, we design a zipper cavity with a resolution of sub-nanometer and a wavelength tunable range of 21 nm. The prototypes of the devices are fabricated and measured. The loss rate is evaluated and the tunability of the wavelength is examined.

1

INTRODUCTION

The spectrometers are indispensable instruments in a wide range of cutting-edge fields. Such as biological sensing, chemical characterization [6], astronomical spectroscopy [2], and remote sensing [1]. The high resolution, high speed, wide operation wavelength, and small size are all wanted features for spectrometers [21].

Recently, lots of efforts have been put into miniaturizing the spectrometers. Compared with the conventional spectrometers which are bulky, the on-chip spectrometers have many advantages. The small size makes it possible to integrate it into portable instruments, which further makes it possible to be used in fields such as real-time health monitoring and pollution detection [14, 30].

Currently, on-chip spectrometers have been realized in various systems, including nanophotonic echelle grating [11], random spectrometers based on disordered scattering [21], metasurfaces [38] and 2D van der Waals materials [39, 44]. However, there are still lots of problems that need to be solved. For example, Risheng Cheng, et. al achieved a broadband spectrometer with a sub-nanometer resolution by echelle gratings [11]. However, a long superconductor nanowire delay line is used to detect the photon and leads to a long dead time. Wladick Hartmann, et. al demonstrated a broadband on-chip spectrometer by disordered scattering. However, the resolution of it is limited by the detector numbers [21]. Achieving an on-chip spectrometer with a broad working wavelength, fast speed, and high resolution is still an intriguing and challenging project. Based on some previous works, the photonic crystals are found to be an ideal platform to achieve this target [32, 40].

Photonic crystals are constructed by material with periodic refractive indices in certain directions [33]. The light propagating through it will be modulated by these periodic refractive indices. This property allows us to modify the interaction between electromagnetic fields and dielectric media [29], which makes them promising candidates for on-chip miniaturized optical components. Among the photonic crystals with different structures, there is a kind of photonic crystals called “zipper cavities”. A zipper cavity is composed of two photonic nanobeam cavities [9, 15]. According to previous works, the zipper cavities have lots of advantages. For instance, they are suitable for a broad range of wavelengths from the visible to the mid-infrared [9]. With careful design, they can have a high optical quality factor [37]. More importantly, with a large optomechanical coupling strength, they have high resonance wavelength tuning rates [34]. These features give them great potential for on-chip broadband high-resolution wavelength tunable filters [12], which further allows us to develop a filter-based on-chip spectrometer with them [27, 42].

The aim of this project is to design an on-chip spectrometer. To realize this purpose, we design a photonic crystal zipper cavity with a tunable resonance wavelength (with a simulated tunable range of more than 20 nanometers). By modifying the optical properties and investigating its optical response, we prove it can serve as a high-resolution (with the sub-nanometer resolution) tunable filter, which makes it possible to serve as the key component of a filter-based on-chip spectrometer. The prototype of the tunable zipper cavity is fabricated and measured. Important optical properties of the cavity such as the external coupling rate and the intrinsic loss rate are evaluated to further optimize the design, and the tunability of the resonance wavelength is proved by comparing the optical responses over the different devices.

In this thesis, we start by introducing the theories used in our works in **chapter 2**. First, we introduce the basic theory of photonic crystal, which directs us in the design of the zipper cavity. The electrostatic force and optomechanical theories are introduced afterward to help us investigate the tunability of the resonance frequency of our cavity. Finally, the input-output theory is introduced to explain how we conduct the measurement and analyze the result.

In **chapter 3**, we introduce how we design the structure of our zipper cavity based on the FEM simulation. Firstly, we introduce how we use the unit cell structure to simulate the 1D photonic crystal constructed by it. By changing the geometry of the unit cell, we can realize a band diagram as we want. After that, we find the unit cells for different regions of the nanobeam and the transition functions to connect them, which helps us to build a full nanobeam cavity. Then, by putting two identical nanobeams together, we make a zipper cavity and simulate the electromagnetic field of its eigenmodes. The tunability of the resonance wavelength induced by changing the internal gap is also evaluated. After we get the zipper cavity we want, we add the electrodes to the model and further simulate the electrostatic force applied to it. The deformation and the change of the eigenmodes induced by this force are evaluated in the following sections and the optomechanical coupling factor is also calculated. Finally, we add a light source to the model and simulate the optical response of the cavity. The FEM simulations in this chapter are conducted with the assistance of COMSOL.

In **chapter 4**, we introduce the experiments we carry out to evaluate the performance of our devices. We first introduce the devices we used in our experiment. After that, we demonstrate the setup for the reflection spectrum, which will be mainly used in the following experiments. Then, we show the reflection spectrum we get and introduce how we extract the resonance wavelength and the total loss rate of the cavity from it. Finally, three we analyze three sets of devices to evaluate the intrinsic loss rate and the external coupling rate, investigate the tunability of resonance wavelength, and demonstrate the operation wavelength ranges of our devices.

2

THEORY

In this chapter, we will introduce the theories used in this thesis. First, we introduce the basic theory of photonic crystal, which gives us the relation between the geometry of the photonic crystal and the electromagnetic fields propagating through it. This directs us in the design of the one-dimensional photonic crystal (1D PhC), which is used as an optical zipper cavity. The electrostatic force and optomechanical theories are introduced in the following sections. The electrostatic force bridges the voltage and the force, and the force will further cause a deformation of the cavity. The optomechanical theories explain the relation between the deformation of the cavity and its resonance frequencies. Therefore, these theories help us in investigating the tunability of the resonance frequency of our cavity when voltage is applied to it. Finally, the input-output theory is introduced. It gives us the relation between the resonance frequencies of the cavity and the optical reflection response of it. This theory helps us to understand how to conduct the measurement and analyze the result.

2.1. BASIC THEORY FOR PHOTONIC CRYSTALS

The photonic crystal is constructed of material with different refractive indices arranged in a periodic structure. This periodic structure gives a periodic potential field that will modulate the electromagnetic (EM) field propagating through it. In the physics picture, the periodic structure gives a periodic permittivity $\epsilon(\mathbf{x})$ and further influences the distribution of the EM field. In this section, we will show that the EM field in photonic crystals is in the form of Bloch waves by following the discussion in [8].

Let's start with the Maxwell's equations, which writes:

$$\begin{aligned} \nabla \cdot \mathbf{D} &= \rho && (2.1)\\ \nabla \cdot \mathbf{B} &= 0 && (2.2)\\ \nabla \times \mathbf{E} &= -\frac{\partial \mathbf{B}}{\partial t} && (2.3)\\ \nabla \times \mathbf{H} &= \mathbf{J} + \frac{\partial \mathbf{D}}{\partial t} && (2.4) \end{aligned}$$

For the PhC, we don't have any free charge or current. Therefore, we should set the charge density ρ and current density $\mathbf{J}$ to be zero. Then the Maxwell's equations writes:

$$\begin{aligned} \nabla \cdot \mathbf{D} &= 0 && (2.5)\\ \nabla \cdot \mathbf{B} &= 0 && (2.6)\\ \nabla \times \mathbf{E} &= -\frac{\partial \mathbf{B}}{\partial t} && (2.7)\\ \nabla \times \mathbf{H} &= \frac{\partial \mathbf{D}}{\partial t} && (2.8) \end{aligned}$$

As the electromagnetic field can always be written written as a sum of time harmonic modes [8] (For example, by Fourier Transformation), we can always write the electric part and magnetic part of the Maxwell's equations as:

$$\begin{aligned} \mathbf{E}(\mathbf{x}, t) &= \mathbf{E}(\mathbf{x}) e^{i\omega t} && (2.9)\\ \mathbf{B}(\mathbf{x}, t) &= \mathbf{B}(\mathbf{x}) e^{i\omega t} && (2.10) \end{aligned}$$

By substituting equations 2.10 and 2.9 into 2.7 and 2.8, we can simplify the Maxwell's equations. In addition, we replace the magnetic field strength $\mathbf{H}$ and electric displacement field $\mathbf{D}$ with the magnetic flux density $\frac{1}{\mu_0}\mathbf{B}$ and the electric field $\epsilon_\mathrm{r}(\mathbf{x})\epsilon_0\mathbf{E}$. The equations can then be written as:

$$\begin{aligned} \nabla \cdot \epsilon_\mathrm{r}(\mathbf{x})\epsilon_0 \mathbf{E}(\mathbf{x}) &= 0 && (2.11)\\ \nabla \cdot \mathbf{B}(\mathbf{x}) &= 0 && (2.12)\\ \nabla \times \mathbf{E}(\mathbf{x}) &= -i\omega \mathbf{B}(\mathbf{x}) && (2.13)\\ \nabla \times \mathbf{B}(\mathbf{x}) &= i\frac{\omega \epsilon_r(\mathbf{x})}{c^2}\mathbf{E}(\mathbf{x}) && (2.14) \end{aligned}$$

Note that with the last two terms in the Maxwell's equations, by substituting the equation 2.14 into 2.13, we can get a function of $\mathbf{B}$:

$$\nabla \times \frac{1}{\epsilon_r(\mathbf{x})} \nabla \times \mathbf{B}(\mathbf{x}) = \frac{\omega^2}{c^2}\mathbf{B}(\mathbf{x}). \qquad (2.15)$$

Then, we can define a Hermitian operator $\hat{\Theta}$:

$$\hat{\Theta}\mathbf{B}(\mathbf{x}) \equiv \nabla \times \frac{1}{\epsilon_r(\mathbf{x})}\nabla \times \mathbf{B}(\mathbf{x}). \tag{2.16}$$

Thus we can rewrite the relation of the **B** fields in equation 2.15 as:

$$\hat{\Theta}\mathbf{B}(\mathbf{x}) = \frac{\omega^2}{c^2}\mathbf{B}(\mathbf{x}). \tag{2.17}$$

Through equation 2.17, we can know that the **B** fields are eigenfunctions of the operator $\hat{\Theta}$ with the eigenvalues of $\frac{\omega^2}{c^2}$.

The equation 2.17 is applicable in any situation. In our situation, e.g., in the photonic crystals, the periodic dielectric structure gives a periodic permittivity. We will then prove that with this periodic permittivity, the **B** fields are governed by Bloch's theorem. Let's first define the translation operator $\hat{T}_R$, which transforms the function in the following way:

$$\hat{T}_\mathrm{R} f(r) \equiv f(r+R). \tag{2.18}$$

In the photonic crystal, the physical structure is periodic, which means the permittivity is also periodic. With **a** denotes the repeating period of the photonic crystal, we can have the relation that:

$$\hat{T}_\mathbf{a}\epsilon(\mathbf{x}) = \epsilon(\mathbf{x}+\mathbf{a}) = \epsilon(\mathbf{x}). \tag{2.19}$$

Consider the translation operators with the subscript of an integral multiple of the repeating period $n\mathbf{a}$, where n is an integer and **a** is the period of the photonic crystal. These operators translate the function with an integral multiple of the period of the photonic crystal. We can prove that these operators $\hat{T}_\mathrm{n\mathbf{a}}$ commute with $\hat{\Theta}$:

$$\hat{T}_\mathrm{n\mathbf{a}}\hat{\Theta}\mathbf{B}(\mathbf{x}) = \hat{\Theta}(\epsilon(\mathbf{x}+\mathrm{n}\mathbf{a}))\mathbf{B}(\mathbf{x}+\mathrm{n}\mathbf{a}) = \hat{\Theta}(\epsilon(\mathbf{x}))\mathbf{B}(\mathbf{x}+\mathrm{n}\mathbf{a}) = \hat{\Theta}\hat{T}_\mathrm{n\mathbf{a}}\mathbf{B}(\mathbf{x}). \tag{2.20}$$

For the operators that have commutation relation $[\hat{\Theta}, \hat{T}_\mathrm{n\mathbf{a}}] = 0$, they have the same eigenfunctions [23]. Therefore, the eigenfunctions of $\hat{\Theta}$, e.g. **B**, can also be obtained by solving the eigenfunctions for translation operator $\hat{T}_\mathrm{n\mathbf{a}}$, which is relatively easier. Considering the eigenvalues $\lambda_\mathrm{n\mathbf{a}}$ for $\hat{T}_\mathrm{n\mathbf{a}}$, two relations need to be met [3]:

$$\int |\hat{T}_\mathrm{n\mathbf{a}}\mathbf{B}(\mathbf{x})|^2 dx = \int |\lambda_\mathrm{n\mathbf{a}}\mathbf{B}(\mathbf{x})|^2 dx = |\lambda_\mathrm{n\mathbf{a}}|^2 \int |\mathbf{B}(\mathbf{x})|^2 dx \tag{2.21}$$

$$\hat{T}_\mathrm{n\mathbf{a}}\hat{T}_\mathrm{m\mathbf{a}}\mathbf{B}(\mathbf{x}) = \lambda_\mathrm{n\mathbf{a}}\lambda_\mathrm{m\mathbf{a}}\mathbf{B}(\mathbf{x}) = \hat{T}_\mathrm{n\mathbf{a}+m\mathbf{a}}\mathbf{B}(\mathbf{x}) = \lambda_\mathrm{n\mathbf{a}+m\mathbf{a}}\mathbf{B}(\mathbf{x}) \tag{2.22}$$

These two relations require the translation operator to have the eigenfunctions in the form of $e^{i\mathbf{k}\cdot\mathbf{x}}$ with eigenvalues e^{ikna}. We notice that for the eigenfunctions with wavevectors k and $k + n * 2\pi/a$, the eigenvalues are the same. Therefore, we can have that:

$$\begin{aligned} \mathbf{B}_{\mathrm{k}}(\mathbf{x}) &= \sum_n \mathbf{B}_{\mathrm{k,n}}(\mathbf{x}) e^{i(k+n*2\pi/a)x} && (2.23)\\ &= e^{ikx}\mathbf{u}_{\mathrm{k}}(\mathbf{x}) && (2.24) \end{aligned}$$

Where $\mathbf{u}_{\mathrm{k}}(x)$ is a periodic function obtained from the sum of the eigenfunctions of the translation operator.

Equation 2.24 is called Bloch theorem [26]. Analogous to solid-state physics, it states that the **B** fields can be written as plane waves modulated by periodic functions. The resulting **B** fields have a period of $2\pi/a$ in k-space and are symmetric at $k = 0$ [8]. Therefore, when studying the **B** fields, we only need to consider the wavevectors that meet $0 < k < \pi/a$, which is called the first Brillouin zone.

Although the $\hat{\Theta}$ operator has the same eigenfunctions as the translation operator, the eigenvalues are still needed to be derived. By substituting the equation 2.24 into equation 2.17, we can get the new relation:

$$(ik\hat{\mathbf{x}} + \nabla) \times \frac{1}{\epsilon_r(\mathbf{x})}(ik\hat{\mathbf{x}} + \nabla) \times \mathbf{u}_{\mathrm{k}}(\mathbf{x}) = \frac{\omega^2(k)}{c^2}\mathbf{u}_{\mathrm{k}}(\mathbf{x}). \tag{2.25}$$

In addition, the boundary conditions need to be met:

$$\begin{aligned} (ik\hat{\mathbf{x}} + \nabla) \cdot \mathbf{u}_{\mathrm{k}}(\mathbf{x}) &= 0 && (2.26)\\ \mathbf{u}_{\mathrm{k}}(\mathbf{x}) &= \mathbf{u}_{\mathrm{k}}(\mathbf{x} + n\mathbf{a}) && (2.27) \end{aligned}$$

Equation 2.26 is derived from Gauss's law for magnetism and equation 2.27 refers to the periodic condition [19]. We can see that for each wavevector k, we should have infinite eigenvalues $(\omega(k)/c^2)_{\mathrm{m}}$, continuous in k-space, but discretely spaced in m [8]. With the assistance of numerical solver tools, we can obtain the eigenfunctions (EM field) and eigenvalues $(\omega(k)/c^2)$. For the continuous wavevector k from 0 to π/a, we can have the corresponding continuous $\omega(k)$. This relation between ω and k is called the optical band diagram of the photonic crystal, in analogy with the electron band diagram in solid-state physics [26]. For each integer m, we have $\omega_{\mathrm{m}}(k)$ continue in k-space, which is called an optical band. The band of $\omega_{\mathrm{m}}(k)$ is called the m^{th} band and the first band $\omega_1(k)$ denotes the one with the lowest frequency. The region between different optical bands is called the band gap.

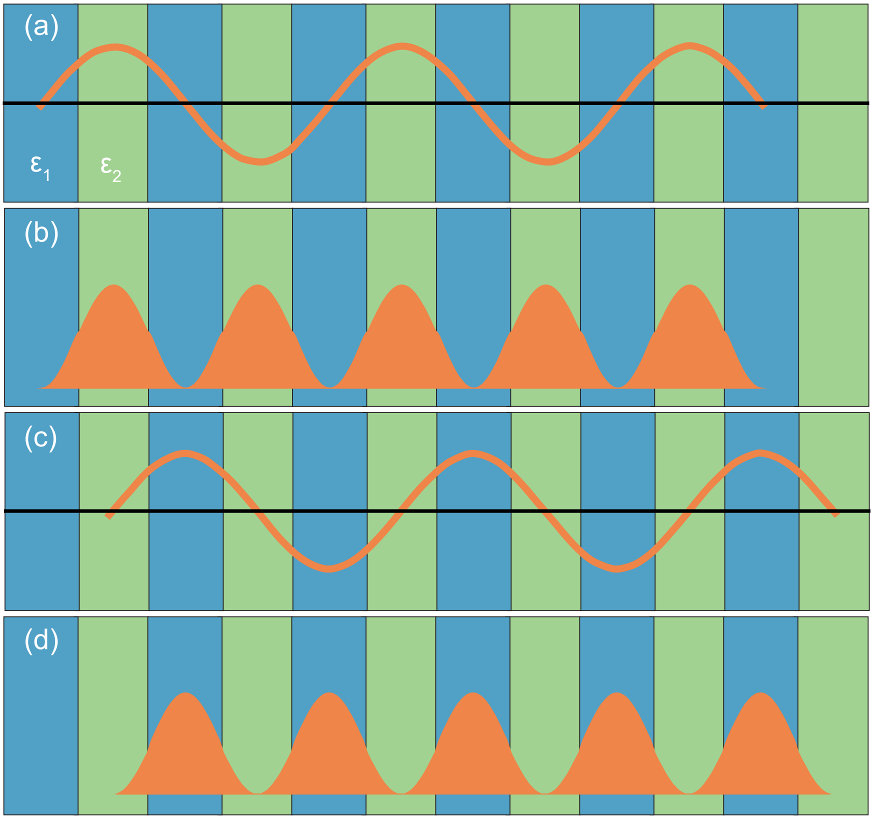

Figure 2.1: (a) Electromagnetic field distribution of the first eigenmode in 1D PhC constructed by two materials with different refraction indices. (b) The $|E|^2$ distribution of the same mode. (c) and (d) The electric field and energy distribution of the air mode. Figures are cited from [23].

One of the most important properties of the photonic crystal is its band gap. As we proved above, the electromagnetic field is Bolch waves in photonic crystals, we can just consider the first Brillouin zone. Specifically, we can consider the situation with wavevector $k = \pi/a$, where is the physical boundary of two different materials. In this paper, one-dimensional photonic crystal (1D PhC) is used for the design of the device. The 1D PhC means that the periodic modulation only happens in one direction, while in other directions, light is free or bounded by some simple dielectric boundary without the period, as shown in Fig. 2.1. The relation between the wavelength of the fundamental mode and the period of the PhC can be described by the following equation [43]:

$$n_1 d_1 + n_2 d_2 = \frac{\lambda}{2}, \tag{2.28}$$

where n_1, n_2 and d_1, d_2 denote the refraction indices and the widths of the first and second material of the PhC, respectively. In addition, the band gap is maximized when the thickness of the two different dielectric materials meets $n_1 d_1 = n_2 d_2$ [23]. Substituting this relation into the equation 2.28, the optimal theoretical thicknesses of the layers are written as:

$$d_1 = \frac{\lambda}{4n_1}, d_2 = \frac{\lambda}{4n_2}. \tag{2.29}$$

Here in our situation, the target wavelength is 1550 nm, and the refraction indices for silicon nitride and air are 2 and 1, respectively [17]. Therefore, the theoretical widths for the two materials are 193.75 nm and 387.5 nm, respectively.

With wavevector $k = \pi/a$, there are two different possible eigenmodes in the 1D PhC [23]. One is the fundamental mode introduced above, and the other is the mode with the same wavevector, but the energy is mainly distributed in the air region as shown in Fig 2.1 (c) and (d). This is called the air mode. With different effective permittivity, the frequencies of these two modes are different, and the frequency difference between these two modes is the band gap. The middle frequency ω_m and the band gap size $\Delta\omega$ are used to describe the band gap. They are given by the functions:

$$\omega_m = \frac{n_1 + n_2}{4n_1 n_2} \cdot \frac{2\pi c}{a} \tag{2.30}$$

$$\frac{\Delta\omega}{\omega_m} \approx \frac{\Delta\epsilon}{\epsilon} \cdot \frac{\sin \pi d/a}{\pi} \tag{2.31}$$

With these functions, we can estimate that for our silicon nitride 1D PhC, we can have a band gap for about 26 THz around our target frequency 193 THz.

2.2. ELECTROSTATIC FORCE

To achieve a photonic crystal cavity with tunable resonance frequency, external control of the system is necessary. The eigenfrequency of the photonic crystal is dependent on its effective ϵ, which is decided by its physical structure [45]. The most straightforward way to modify the effective ϵ is to induce some deformation in the physical structure [34]. However, the scale of our system is in hundreds of micrometers, which means it's extremely difficult to apply forces on it. In this case, the electrostatic force becomes an ideal candidate, which makes it possible to apply forces on a tiny structure by just depositing metallic on our photonic crystals and apply a voltage on it [5]. Moreover, the magnitude force is easily to control by simply changing the input voltage.

The principle for the electrostatic force is relatively simple. For a capacitor with capacitance C, the relation between the voltage V and the energy stored on it follows the formula [19]:

$$W_\mathrm{e} = \frac{1}{2} C V^2, \tag{2.32}$$

where W_e is the charging energy. Considering a parallel-plate capacitor, the capacitance of it can be written as:

$$C = \frac{\epsilon A}{d}, \tag{2.33}$$

where ϵ, A, and d refer to the permittivity, capacitor area, and the distance between two parallel plates. Therefore, the charging energy can be written as:

$$W_\mathrm{e} = \frac{1}{2}\frac{\epsilon A V^2}{d}. \tag{2.34}$$

While the force can be derived by the derivation between the energy and displacement, it can be written as:

$$F = \frac{\partial W_\mathrm{e}}{\partial d} = -\frac{1}{2}\frac{\epsilon A V^2}{d^2}. \tag{2.35}$$

From the formula, we can see that with certain material, the electrostatic force is proportional to the plate area, the square of the applied voltage, and inverse proportional to the square of the plate gap. In our cases, the permittivity and the initial distance are relatively fixed. The area can be controlled by the length and thickness of the metal deposition. The voltage is the main parameter that we will control to induce the deformation and control the resonance frequency of our cavity.

2.3. OPTOMECHANICS

The optomechanical theory is used to describe the system in which optics and mechanics both play important roles. When describing an optomechanical system, the interaction term between the optics and mechanics in quantum mechanics description is [4]:

$$\hat{H}_\mathrm{int} = \hbar g_0 \hat{a}^\dagger \hat{a}(\hat{b} + \hat{b}^\dagger), \tag{2.36}$$

where $\hat{a}$, $\hat{b}$ ($\hat{a}^\dagger$, $\hat{b}^\dagger$) refer to the annihilation (creation) operators of the optics and mechanics systems, respectively. The parameter g_0 is called single-photon optomechanical coupling strength, which describes the strength of the interaction between photon and phonon [4]. The expression of g_0 can be written as:

$$g_0 = G \cdot x_\mathrm{ZPF}\,, \text{ where } G = \frac{\partial \omega}{\partial x}, \tag{2.37}$$

where the G is the optomechanical coupling factor which evaluates the optical frequency shift per displacement, while the x_ZPF is the zero-point fluctuation [4]. However, in our system, the mechanical deformations are not decided by the mechanical eigenmodes,

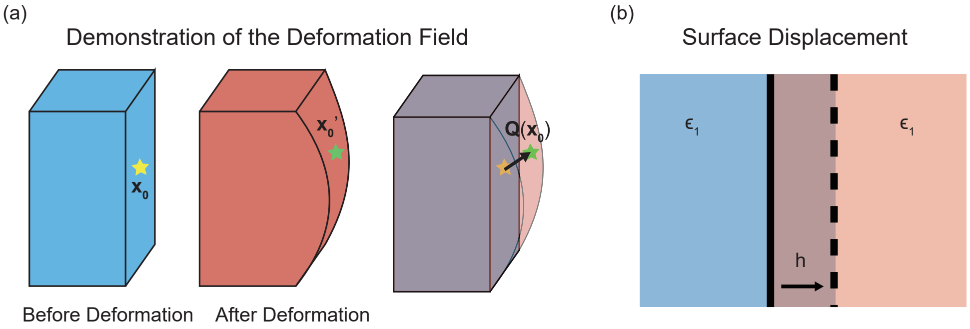

Figure 2.2: (a) The demonstration of the deformation field $\mathbf{Q}(\mathbf{x})$. (b) The boundary between two different dielectric materials in a small region.

which are related to the zero point fluctuation. Therefore, we only care about the G factor which gives us the relation between the frequency shift of the system and the deformation. The deformation will be evaluated by electrostatic force with the assistance of the FEM simulator.

To evaluate the magnitude of the G factor, we will introduce the Moving Dielectric Boundary theory. The Moving Dielectric Boundary theory is based on the perturbation theory and evaluates the shift of the frequency induced by the changing of effective permittivity caused by the deformation of the system [8]. Therefore, this theory works in both the quantum regime and macro scale [4].

Before introducing the Moving Dielectric Boundary theory, we need to give some definitions. Considering a three-dimensional system, the deformation of the system can be described by a vector field $\mathbf{Q}(\mathbf{x})$, where $\mathbf{x}$ is a vector that represents the position of a point before the deformation happens. Considering a point $\mathbf{x_0}$ before the deformation, after the deformation happens, the point will move to a new position $\mathbf{x_0'}$. The displacement between $\mathbf{x_0}$ and $\mathbf{x_0'}$ is expressed by $\mathbf{Q}(\mathbf{x_0})$. The sketch of this explanation is shown in Fig. 2.2 (a) to give a more clear picture. Then, we can further parameterize the displacement field for the convenience of further calculation. For a small enough displacement field that can be regarded as a perturbation, we can write the vector field $\mathbf{Q}(\mathbf{x})$ as the production as the perturbation magnitude α and the normalized displacement field $\mathbf{q}(\mathbf{x})$, which is $\mathbf{Q}(\mathbf{x}) = \mathbf{Q}(\alpha, \mathbf{x}) = \alpha\mathbf{q}(\mathbf{x})$. In addition, the relative permittivity can also be written as a scale field $\epsilon(\mathbf{x})$ with $\mathbf{x}$ denoting the coordinate.

Through the perturbation theory, the shift of the frequency of the system induced by a tiny perturbation on the effective permittivity can be written as:[16]

$$\frac{d\omega}{d\alpha} = -\frac{\omega_0}{2}\frac{\langle \mathbf{E}(\mathbf{x})|\frac{d\epsilon(\mathbf{x})}{d\alpha}|\mathbf{E}(\mathbf{x})\rangle}{\langle \mathbf{E}(\mathbf{x})|\epsilon(\mathbf{x})|\mathbf{E}(\mathbf{x})\rangle} = -\frac{\omega_0}{2}\frac{\int d\mathbf{x}\frac{d\epsilon(\mathbf{x})}{d\alpha}|\mathbf{E}(\mathbf{x})|^2}{\int d\mathbf{x}\epsilon(\mathbf{x})|\mathbf{E}(\mathbf{x})|^2}. \tag{2.38}$$

Now, the relation between the permittivity and the perturbation still needs to be investigated. To simplify the model, we will begin with the one-dimensional system. Considering the boundary of two different dielectric materials shown in Fig. 2.2 (b), the permittivity in a one-dimensional system can be demonstrated by a Heaviside function $\Theta(x)$. For a system with two different materials with permittivity ϵ_1 and ϵ_2, while setting the boundary between these two materials at x_0, the permittivity should be ϵ_1 for $x < x_0$ and ϵ_2 when $x > x_0$. To meet this requirement, the permittivity of this system can be written as:

$$\epsilon(x) = \epsilon_1 + (\epsilon_2 - \epsilon_1)\Theta(x - x_0 - Q(\alpha, x_0)). \tag{2.39}$$

In addition, the derivation of the Heaviside function is the delta function. Therefore, the numerator of the perturbation theory can be written as:

$$\begin{aligned}
\langle \mathbf{E}(x)|\frac{d\epsilon(x)}{d\alpha}|\mathbf{E}(x)\rangle &= \langle \mathbf{E}(x)|\frac{d\epsilon(x)}{dQ(\alpha,x_0)}\frac{dQ(\alpha,x_0)}{d\alpha}|\mathbf{E}(x)\rangle && (2.40)\\
&= \int dx(\epsilon_2-\epsilon_1)\delta(x-x_0-Q(\alpha,x_0))\frac{dQ(\alpha,x_0)}{d\alpha}|\mathbf{E}(x)|^2 && (2.41)\\
&= \frac{dQ(\alpha,x_0)}{d\alpha}(\epsilon_2-\epsilon_1)|\mathbf{E}(x)|^2\,|_{x=x_0} && (2.42)
\end{aligned}$$

Then, considering a three-dimensional system, the boundary now becomes a surface with the coordinates (x, y, z). In addition, only the displacement perpendicular to the surface will lead to a change in the distribution of the permittivity of the whole system. Therefore, the term $Q(\alpha, x)$ is converted to $\mathbf{Q}(\alpha, x, y, z) \cdot \hat{\mathbf{n}}(x, y, z)$, where $\hat{\mathbf{n}}$ denotes the normalized surface vector. Replacing the result by surface integration, the formula in the three-dimensional situation then becomes:

$$\langle \mathbf{E}(\mathbf{x})|\frac{d\epsilon(\mathbf{x})}{d\alpha}|\mathbf{E}(\mathbf{x})\rangle = \oint_A dA\frac{d\mathbf{Q}(\alpha,x,y,z)\cdot\hat{\mathbf{n}}(x,y,z)}{d\alpha}(\epsilon_2-\epsilon_1)|\mathbf{E}(\mathbf{x})|^2. \tag{2.43}$$

This function gives a form to derive the relation between the resonance and the deformation. However, the electric field here is not well defined. To be more specific, the surface integration requires the electric field at the boundary. However, the perpendicular component of the electric field on the surface is discontinued, which must obey the relation $\epsilon_1\mathbf{E}_{\perp,1} = \epsilon_2\mathbf{E}_{\perp,2}$ [19]. Neither $\mathbf{E}_{\perp,1}$ nor $\mathbf{E}_{\perp,2}$ is proper to be substituted into equation 2.43. Therefore, a more careful insight into the small area around the dielectric boundary is needed to solve this problem. One way for solving this problem is given by Steven G. Johnson, et al [24].

To avoid the discontinuity on the boundary, we consider the permittivity as a matrix, which allows us to separate the perpendicular terms and the in-plane terms:

$$\epsilon = \begin{pmatrix} \tilde{\epsilon} & 0 & 0 \\ 0 & \overline{\epsilon} & 0 \\ 0 & 0 & \overline{\epsilon} \end{pmatrix} \tag{2.44}$$

Here the $\tilde{\epsilon}$ refers to the perpendicular terms while the $\bar{\epsilon}$ refers to the in-plane terms.

We can start with the in-plane components of the permittivity, which don't need to meet the continuous restriction and are easier to due with. Considering a small area in the surface dA, recall that we always have the relation $\epsilon(x) = \epsilon_1 + (\epsilon_2 - \epsilon_1)\Theta(x-h)$ (here we set the x_0 to be 0 for convenience, and h denotes a small displacement of the boundary as shown in Fig. 2.2 (b)). This time, we start with a relatively smooth boundary transition and then go to the limit which is a Heaviside function transition. The permittivity in a smooth transition is denoted as ϵ_s. In this case, looking at the region around the boundary, the in-plane component of the permittivity in this small region can be written as:

$$\bar{\epsilon}_s(x) = \int g_s(x-x')\epsilon(x')dx', \tag{2.45}$$

where g_s is a smooth transition function with the property:

$$\int_{-\infty}^{\infty} g_s(x)dx = 1 \tag{2.46}$$

$$\lim_{s\to 0} g_s(x) = \delta(x) \tag{2.47}$$

The plot of the g_s function is shown in Fig. 2.3. In this way, we can get the derivation of the permittivity is that:

$$\frac{d\bar{\epsilon}_s(x)}{dh} = (\epsilon_2 - \epsilon_1)g_s(x-h). \tag{2.48}$$

Remind that this transition relation doesn't meet the continuous requirement in a perpendicular direction. Therefore, a function which can describe the transition and the continuity of the permittivity simultaneously is needed. Fortunately, a proper function has already been found in previous works [25, 31]:

$$\tilde{\epsilon}_s(x)^{-1} = \int g_s(x-x')\epsilon(x')^{-1}dx'. \tag{2.49}$$

And again, the derivation relation can be written as:

$$\frac{d\tilde{\epsilon}_s(x)}{dh} = -\tilde{\epsilon}_s(x)^2\,(\frac{1}{\epsilon_2} - \frac{1}{\epsilon_1})g_s(x-h). \tag{2.50}$$

Now we have the permittivity for different directions. By combining it with the corresponding electric field components, we can get a new form of the numerator of the perturbation theory:

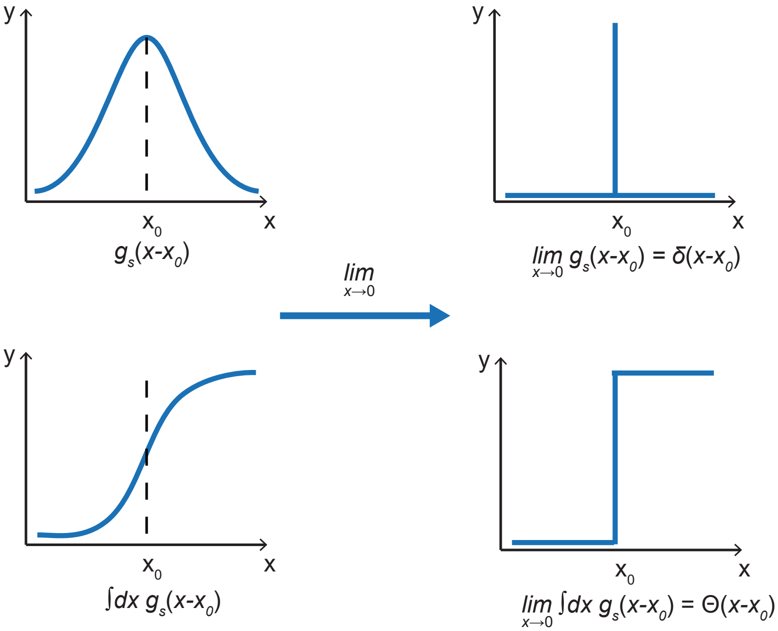

Figure 2.3: The plot of g_s and its integral in normal condition and at the limit of $s \to 0$.

$$\langle \mathbf{E}(x)|\frac{d\epsilon_s(x)}{d\alpha}|\mathbf{E}(x)\rangle = \langle \mathbf{E}(x)|\frac{d\epsilon_s(x)}{dh}\frac{dh}{d\alpha}|\mathbf{E}(x)\rangle \tag{2.51}$$

$$= dA\frac{dh}{d\alpha}\int dx((\epsilon_2-\epsilon_1)|\mathbf{E}_\parallel|^2-(\frac{1}{\epsilon_2}-\frac{1}{\epsilon_1})|\tilde{\epsilon}_s(x)\mathbf{E}_\perp|^2)g_s(x-h) \tag{2.52}$$

Considering the limit of the g_s, the g_s becomes a delta function at $s \to 0$. And the smoothed permittivity becomes the permittivity in the real situation [31]. In addition, remember that in previous steps, the form of $g_s(x-h)$ is the simplified form by considering the boundary at the origin of the coordinate. In the real situation, the actual form should be $g_s(x-h-x_0)$ for a small surface area. Then the complete version of the function can be written by the surface integration as:

$$\oint_A dA\frac{dh(\alpha,x,y,z)}{d\alpha}((\epsilon_2-\epsilon_1)|\mathbf{E}_\parallel(x,y,z)|^2-(\frac{1}{\epsilon_2}-\frac{1}{\epsilon_1})|\epsilon(x,y,z)\mathbf{E}_\perp(x,y,z)|^2). \tag{2.53}$$

Finally, for the whole formula, the final expression for the G factor is given by:

$$\left.\frac{d\omega}{d\alpha}\right|_{\mathrm{mb}} = -\frac{\omega_0}{2}\frac{\oint_A dA\mathbf{q}(x,y,z)\cdot\hat{\mathbf{n}}(x,y,z)(\Delta\epsilon|\mathbf{E}_\parallel(x,y,z)|^2-\Delta\epsilon^{-1}|\mathbf{D}_\perp(x,y,z)|^2)}{\int dx\epsilon(\mathrm{x})|\mathbf{E}(\mathrm{x})|^2}, \tag{2.54}$$

where $\Delta\epsilon = \epsilon_2-\epsilon_1$ and $\Delta\epsilon^{-1} = \frac{1}{\epsilon_2}-\frac{1}{\epsilon_1}$.

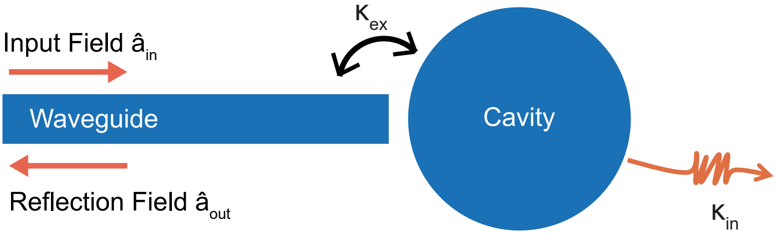

Figure 2.4: The simplified sketch of the 1-port cavity, which is constructed by the port (waveguide) and the cavity.

Until now, we can derive the *G* factor from the deformation field and electric field, which can be obtained from the simulation which will be introduced in the later part of this thesis. The G factor evaluates how large the shift of the frequency will be with a small perturbation. It's an important tool for us to theoretically analyze how sensitive the resonance frequency of our device is to the deformation in the following chapters.

2.4. INPUT-OUTPUT THEORY

The cavity's response to the input light is described by the input-output theory model [4]. In this section, we will introduce the input-output theory, which will give us the relation between the cavity's reflection response, input frequency, cavity resonance frequency, and coupling strength.

Considering a cavity connected to a waveguide with a resonance at ω_c as shown in Fig. 2.4, there are two ways that the light will be lost from the cavity [7]. One way is by coupling to the waveguide. The loss rate of this way is described by the external coupling rate κ_{ex}. The other way is the internal loss of the cavity itself, such as the leaking into the environment, and the thermal absorption by the cavity. The loss rate in this way is described by the intrinsic loss rate κ_{in}.

The input-output theory is based on the Heisenberg equations of motion [20]. In the Heisenberg equation, the field in the cavity is described by the operator $\hat{a}$. The time evolution of the cavity annihilation operator can be written as [4]:

$$\dot{\hat{a}} = -\frac{\kappa}{2} + i\Delta\hat{a} + \sqrt{\kappa_{\mathrm{ex}}}\hat{a}_{\mathrm{in}}, \tag{2.55}$$

where the Δ is the detuning between the input signal and the cavity resonance frequency, which can be written as $\omega_{\mathrm{in}} - \omega_{\mathrm{c}}$. The κ is the total loss rate which is the sum of all the losses $\kappa = \kappa_{\mathrm{in}} + \kappa_{\mathrm{ex}}$. The $\hat{a}_{\mathrm{in}}$ is the annihilation operator of the input field. The output field of this cavity can be written as:

$$\hat{a}_{\mathrm{out}} = \hat{a}_{\mathrm{in}} - \sqrt{\kappa_{\mathrm{ex}}}\hat{a}. \tag{2.56}$$

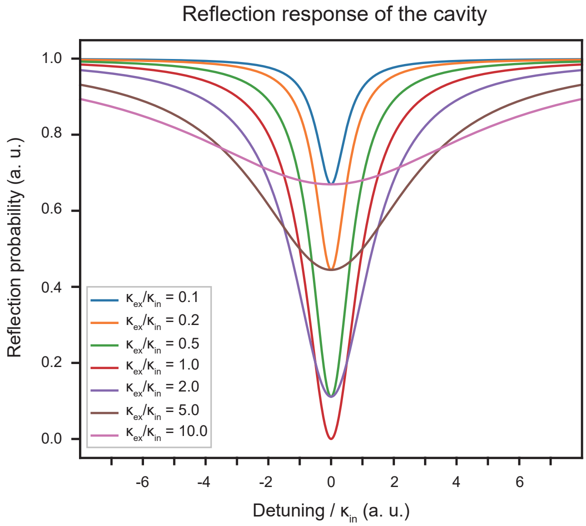

Figure 2.5: The plot of the reflection response of the cavity with different ratios between κ_{in} and κ_{ex}

As we are considering the stationary state, in which the time derivation of the cavity field operator is zero, which means the equation 2.55 equals to zero. In addition, the actual amplitude of the field is given by the average of the operator, namely, $\langle\hat{a}\rangle$ [4]. By eliminating $\hat{a}$, we can get a ratio between the $\hat{a}_{\text{in}}$ and $\hat{a}_{\text{out}}$, e.g., the reflection amplitude R. The result can be written as:

$$R = \frac{\langle\hat{a}_{\text{out}}\rangle}{\langle\hat{a}_{\text{in}}\rangle} = \frac{(\kappa_{\text{in}} - \kappa_{\text{ex}})/2 - i\Delta}{(\kappa_{\text{in}} + \kappa_{\text{ex}})/2 - i\Delta}. \tag{2.57}$$

This formula gives the relation between the input and the reflection fields. In the real situation, the signal we detect is the intensity of the light, which is proportional to the probability of reflection from the cavity and can be written as $|R|^2$. The reflection probability then can be written as:

$$|R|^2 = 1 - \frac{\kappa_{\text{in}}\kappa_{\text{ex}}}{(\frac{\kappa_{\text{in}}+\kappa_{\text{ex}}}{2})^2 + \Delta^2}. \tag{2.58}$$

We can see that the reflection probabilities are decided by both the intrinsic loss rate, the external coupling rate, and the detuning. The plot of the reflection probabilities is shown in Fig. 2.5. The reflection probabilities reach their minimum at $\Delta = 0$, and with a large detuning, they will converge to one. In addition, when $\kappa_{\text{in}} = \kappa_{\text{ex}}$, the reflection probability goes to zero when the input light is on resonance. This condition is called critical coupling. When the external coupling rate increases, the linewidth of the curve increases. Oppositely, when the intrinsic loss rate increases, the linewidth will decrease.

3

DESIGN AND SIMULATION

In this chapter, we introduce our procedure to design the zipper cavity, which can serve as the key component of an on-chip spectrometer device. The 1D PhC is a periodic structure constructed by repeating the unit cell along a certain direction. Therefore, the first step for designing the 1D PhC is to find an ideal unit cell structure. We start with the design of the photonic crystal unit cell in section 3.1. By studying the influence of different geometry parameters on the eigenfrequency, we learn how to control the band diagram by changing the geometry of the unit cell. After that, we design unit cells with desired eigenfrequencies. With transition functions, we make a nanobeam cavity in section 3.2. However, the nanobeam is barely tunable, which makes it impossible to construct a spectrometer device with it. Therefore, in section 3.3, by putting two identical nanobeams together, we construct a zipper cavity, whose eigenfrequencies can be tuned by changing the distance between two nanobeams. To tune the internal gap distance of the cavity, we need to apply force to it. In section 3.4, we conduct the electrostatic force simulation to evaluate the deformation induced by the voltage applied to it. Then in the following section 3.5, we combine the electrostatic force simulation and the optics simulation. We study the eigenmode of the deformation structure and derive the optomechanical coupling factor. The simulations until now are all focused on the eigenfrequency of the device, and the response of the device with input sources has not been evaluated. Therefore, in section 3.6, we evaluate the optical response of our system. This helps us predict the performance of our device and find the optimal waveguide-cavity distance, which is difficult to get from the theory.

3.1. PHOTONIC CRYSTAL UNIT CELL

In this section, we introduce the way to design the unit cell for 1D PhC. Firstly, we introduce the geometry parameters that decide the geometry of our unit cell, and the boundary conditions that realize the transverse electromagnetic (TE) modes that are used in the simulation. These help us to set up the model for the FEM simulation. After that, by

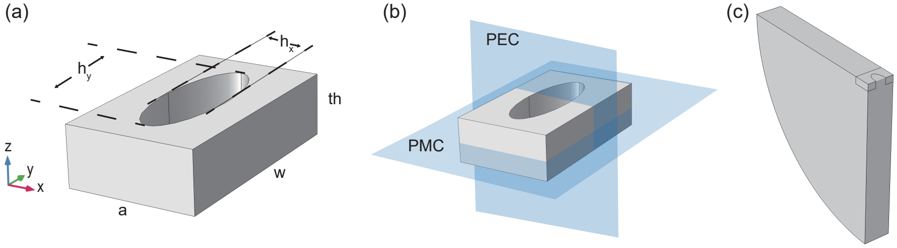

Figure 3.1: (a) The geometry of the photonic crystal unit cell. (b) The boundary conditions applied on the unit cell to realize the TE mode and simplify the simulation. PEC and PMC refer to the Perfect Electric Conductor and the Perfect Magnetic Conductor, respectively. (c) The geometry of the final structure used for the simulation.

conducting simulations and varying different geometry parameters, we show how the eigenfrequency is influenced by the change of the unit cell geometry, which enables us to further control the eigenfrequency of the photonic crystal.

In our case, we set the x-axis as the repeating direction. Following the example of Jasper Chan et al, the structure of the PhC unit cell is constructed by a rectangular silicon nitride bulk with an ellipsoid air hole in the center of it [10]. The structure of the unit cell is shown in Fig 3.1 (a). For this structure, there are 5 parameters to decide the geometry of the unit cell. The length of the unit cell a and the width of the unit cell w decide the geometry of the rectangle silicon nitride bulk. In addition, as a is the length along the x direction, which is the repeating direction of the 1D PhC, it also represents the lattice constant of the PhC. The variables h_x and h_y represent the width of the ellipse along the x-axis, and the height of the ellipse along the y-axis, respectively, which decide the geometry of the air hole. Finally, th represents the thickness of the unit cell in the z-direction. These 5 parameters together decide the geometry of the unit cell.

By changing the parameters in a reasonable range, we can change the geometry of our unit cell. Considering the fabrication condition, the thickness of the PhC depends on the thickness of the silicon nitride layer, which has been grown previously and is not easy to change. However, all the other four parameters are flexible which makes it possible to realize the ideal photonic band structure. The only limitation of these parameters is the minimum feature size which is restricted by the accuracy of fabrication and the robustness of the device. According to the experience of fabrication, the smallest feature of the device should be larger than 80 nanometers. The initial geometry parameters are taken from the paper of Jasper Chan et al in 2012 [10]. The value of the parameter set $(a, w, h_\mathrm{x}, h_\mathrm{y})$ in nanometer is (440, 530, 170, 370).

As transversal electric mode (TE mode) is used in our device, we need some boundary conditions to restrict the electromagnetic field to realize this mode. As the propagation direction of the TE wave is along the x-axis, the ideal mode should have zero electric fields along the x-axis and the z-axis. In addition, the electromagnetic field should be symmetric in the y and z directions. To realize these conditions in the simulation, we

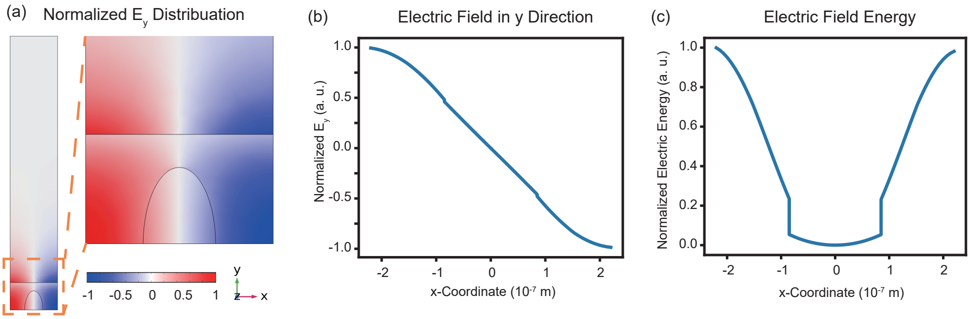

Figure 3.2: (a) The spatial distribution of the y component of the electric field for the eigenmode. (b) and (c) The spatial distribution of the electric field and electric energy.

divide the unit cell, apply boundary conditions, and simulate a quarter of it, which allows us to meet the symmetric conditions and eliminate unwanted components of the electromagnetic fields. The Perfect Electric Conductor (PEC) condition is applied to the z-x symmetric plane of the model and the Perfect Magnetic Conductor (PMC) condition is applied to the x-y symmetric plane of the model. The detailed resonance for applying boundary conditions in this way and how it leads to a TE mode is further explained in appendix A.1. Moreover, to make the simulation consistent with the realistic condition, we add an air cylinder to imitate the environment around the device. The boundary outside the air cylinder is set as a scattering boundary to let the light pass through and propagate to the infinite far without reflection. Finally, periodic conditions are applied to both sides of the unit cell to get a continuous wavevector. The boundary conditions applied in the model and the final geometry are demonstrated in Fig. 3.1 (b) and (c).

With the simulation strategy mentioned above, we can simulate the electromagnetic fields of the photonic crystal constructed by infinite unit cells repeated in the x direction. Three simulations are done to study the electric field distribution and the optical band diagram of the photonic crystal. Firstly, we simulate the electromagnetic field distribution of the eigenmode with a wavevector of π/a The field distribution of the TE mode is shown in Fig. 3.2 (a), which is consistent with the distribution mentioned in Chan's paper. The spatial distribution of electric field and electric energy are shown in Fig. 3.2 (b) and (c). As shown in the theoretical section, the electric energy is distributed mainly inside the silicon nitride. A sharp transition in the boundary between the air and silicon nitride also appeared in the energy plot. With these results, we show that we already have a reasonable mode according to the electric field distribution, and we can move to analyze the band diagram.

Then, we simulate the band diagram of the unit cell with different h_x while other parameters are fixed. This helps to understand how the band diagram changes according to the change of this geometry parameter. The optical band diagram of the photonic crystal is illustrated in Fig. 3.3 (a). The band with the lower frequency ended at about 272 THz with the wavevector of π/a. In addition, a clear band gap can be seen between the first

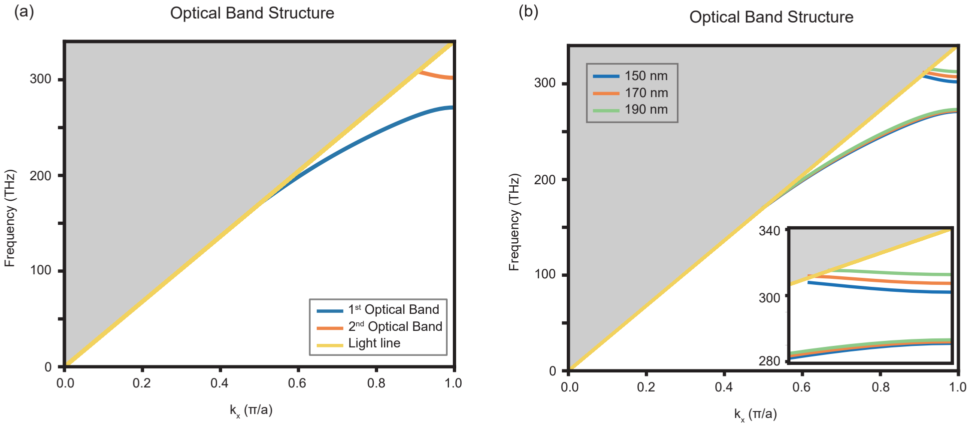

Figure 3.3: (a) The band structure of the sample with the original parameters. (b) The change of the first and second optical bands with different h_x. The zoom-in figure is inserted into it.

and second optical bands within the area under the light line. By changing the width of the air hole h_x, the band diagram changes with it. Fig. 3.3 (b) shows the change of the band with different h_x. We can see the eigenfrequencies of both the first and second bands increase with increasing h_x.

Finally, with the same method, we simulate the band diagram when the other 3 parameters are changed. As what we do to evaluate the influence of changing h_x, when we change one parameter, we keep the other parameters fixed. The changes of the positions of the first and second bands with different parameters varied are demonstrated in Fig. 3.4. We can see that the eigenfrequency is correlated with the h_x and h_y while anti-correlated with a and w. The result is consistent with the fact that as silicon nitride has a higher refractive index, with a larger silicon nitride proportion, the supported frequency will decrease. Oppositely, with larger air proportion, the frequency increases. With this result, we learn about the influence of different parameters on the band gap of the photonic crystal, which further enables us to design photonic crystals with certain band diagrams.

3.2. ONE-DIMENSIONAL PHOTONIC CRYSTAL NANOBEAM

With all the knowledge gained above, we can modify the band diagram by changing the geometry parameters. In this section, we introduce how we find proper unit cells for a nanobeam cavity and how to constitute the nanobeam with them. We start with the introduction of the nanobeam and show the requirements of the band diagrams of its unit cells. After that, we show the transition functions that govern the transition of the sizes of the unit cells that construct the nanobeam. Then we conduct the simulation and optimization. We show the band diagrams of the unit cells we designed based on

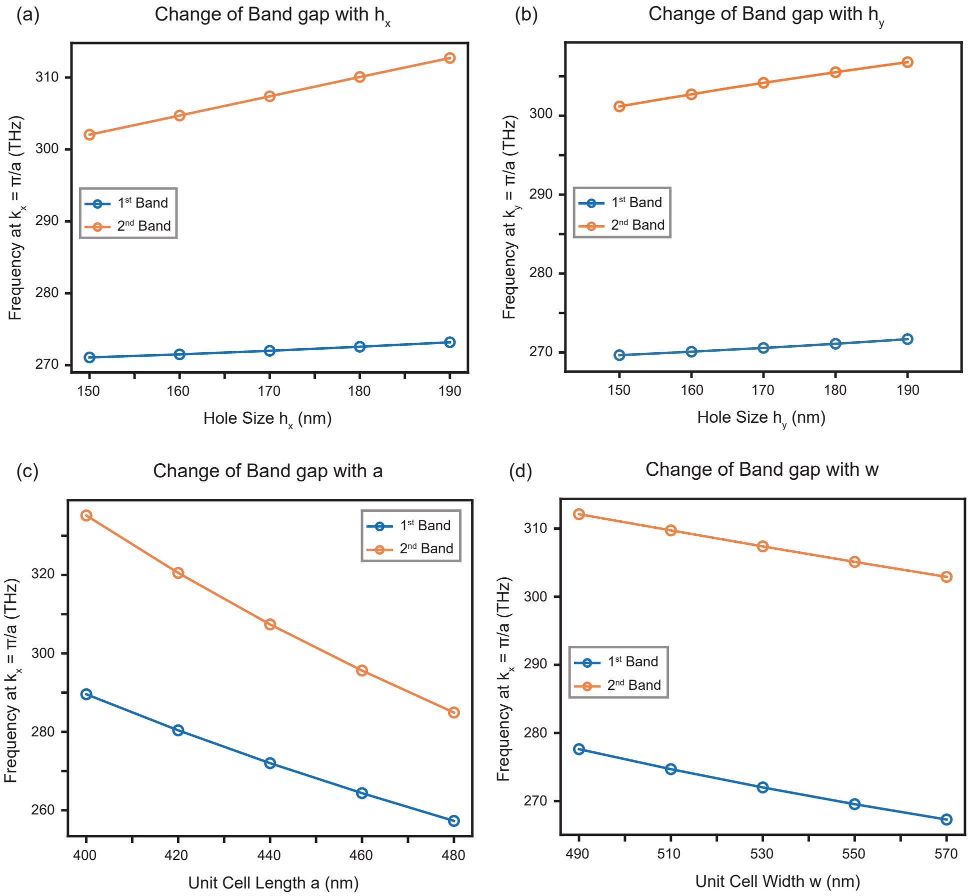

Figure 3.4: The change of the first and second band with the change of different parameters. The frequencies represent the mode with wavevector of π/a.

the requirement of the nanobeam. Finally, with the transition functions we get from the optimization, we demonstrate the full nanobeam structure and its electromagnetic properties.

The nanobeam cavity is a kind of one-dimensional photonic crystal which can confine the light with a certain frequency in the center of it [28]. It is constituted by two different regions, which we call the mirror region and the defect region. The defect region is in the center of the photonic crystal while the mirror regions are on both sides of it. To confine the light in a certain area, we need two kinds of unit cells with different band diagrams for these two regions. The geometry arrangement and corresponding ideal band diagram are shown in Fig. 3.5 (a). For the defect region, we want unit cells whose first band is at the target frequency, so that the light of the target frequency can propagate in this region. For the mirror regions on both sides of it, we need unit cells with a band gap around the target frequency. Therefore, the light of the target frequency cannot propagate through these regions and will be reflected. These regions work like mirrors that can prevent the light with target frequency from leaking out of the defect region. With this arrangement, the light can be confined inside the defect region.

Until now, we know that we need the defect region in the middle and the mirror regions on both sides of it. There are still lots of ways to arrange the unit cells for each region. For example, we can construct the mirror regions with identical unit cells whose band diagrams meet the requirement. For the defect region, we can also use identical unit cells whose first band is at the target frequency. In this way, only two kinds of unit cells are used in the whole nanobeam and there will be a significant size change on the boundary of these two regions. In this work, instead, we will use a relatively smooth transition between these two regions. Following the method proposed by Jasper Chan et al, we use a transition function to control the transition of the sizes of the unit cells from the mirror region to the defect region [10]. According to their work, the Gauss function can serve as the transition function. In addition, the defect region should have a higher eigenfrequency, which means it should have a smaller lattice constant than the mirror region (See the theory section and Fig. 3.4). Therefore, the lattice constants of the nanobeam can be written as:

$$a_{\mathrm{n}} = a_{\mathrm{mirror}}\,(1 - c_1 e^{(n-n_{\mathrm{mid}})^2/2c_2^2}), \tag{3.1}$$

where a_{n} notes the lattice constant of the n^{th} unit cell in the nanobeam, n_{mid} marks the middle one of the defect region. Notably, the ratio of the lattice constant between the smallest unit cell and the mirror unit cell is decided by the Gauss parameter c_1. Therefore, we call it the maximum difference. In addition, the other parameter c_2 controls the broadening of the Gauss function, e.g. the shape of the Gauss well function, and it's called the well factor. However, the h_{x} and h_{y} in the defect region may not have the same changing rate as the lattice constant. Therefore, two additional parameters are used to control the change of the hole sizes. The oblongness factor for the x and the y directions are applied and the h_{x} and h_{y} in the nanobeam can be described by the following equations:

$$h_{\mathrm{x,n}} = h_{\mathrm{x,mirror}}\,(1 - c_1 e^{(n-n_{\mathrm{mid}})^2/2c_2^2})^{-obl_x} \tag{3.2}$$

$$h_{\mathrm{y,n}} = h_{\mathrm{y,mirror}}\,(1 - c_1 e^{(n-n_{\mathrm{mid}})^2/2c_2^2})^{obl_y} \tag{3.3}$$

Notably, a minus sign is applied to the oblongness factor in the x direction because of the previous experiences in designing of the nanobeam [22]. An example of these transition functions is shown in Fig. 3.6 (a). While the thickness and the width of the nanobeam should be fixed over the whole beam, the transitions of the other three parameters are governed by these three transition functions. Therefore, by finding the geometry parameters of the unit cells for the mirror and the defect regions, and the three transition functions, we can decide the full geometry of the nanobeam cavity.

With the requirements and method mentioned above, we conduct simulations and optimizations to find the geometry parameters of the unit cells of the mirror and defect regions and the transition functions that govern the transition of the geometry parameters between different regions. Firstly, we simulate the band diagram of the unit cell and adjust the geometry parameters to modify the position and the width of the bandgap. In this way, we realize the desired band diagram for both regions. The results are plotted in Fig. 3.5 (b) and (c). We can see that for the defect region, the first band is located exactly at 193 THz, which is our target frequency. While for the mirror region, there is a band gap from 178 THz to 215 THz, between the first and second bands. These band diagrams meet the requirements for unit cells of the defect and the mirror regions, respectively.

Then with the unit cells we found, we conduct the optimization to find the transition functions for optimal nanobeam structure. The optimization is done with MATLAB scripts with the $fminsearch$ function, which is based on the Nelder–Mead algorithm [36]. In this way, we find the optimal transition functions which give us a nanobeam with a high quality factor, e.g., minimum loss. With these transition functions, we can construct a full nanobeam cavity, whose structure is shown in Fig. 3.6.

Finally, the electromagnetic field simulation is conducted and the electromagnetic field and the energy distribution are also shown in Fig.3.6 (b) and (c). We can see that the electromagnetic field and the electric energy are confined in the middle of the defect region and the field is anti-symmetric along the axis. This helps us to manipulate the optical performance of our device better in the following steps.

3.3. ZIPPER CAVITY

Since now, we have 1D PhC nanobeam which allows us to confine the light in a small mode volume. In this section, we convert the nanobeam into a zipper cavity. We first introduce the properties of the zipper cavities. After that, we simulate the electromagnetic field of the zipper cavity. Finally, we study the shift of the eigenfrequencies with the change of the distance between two nanobeams that construct the zipper cavity.

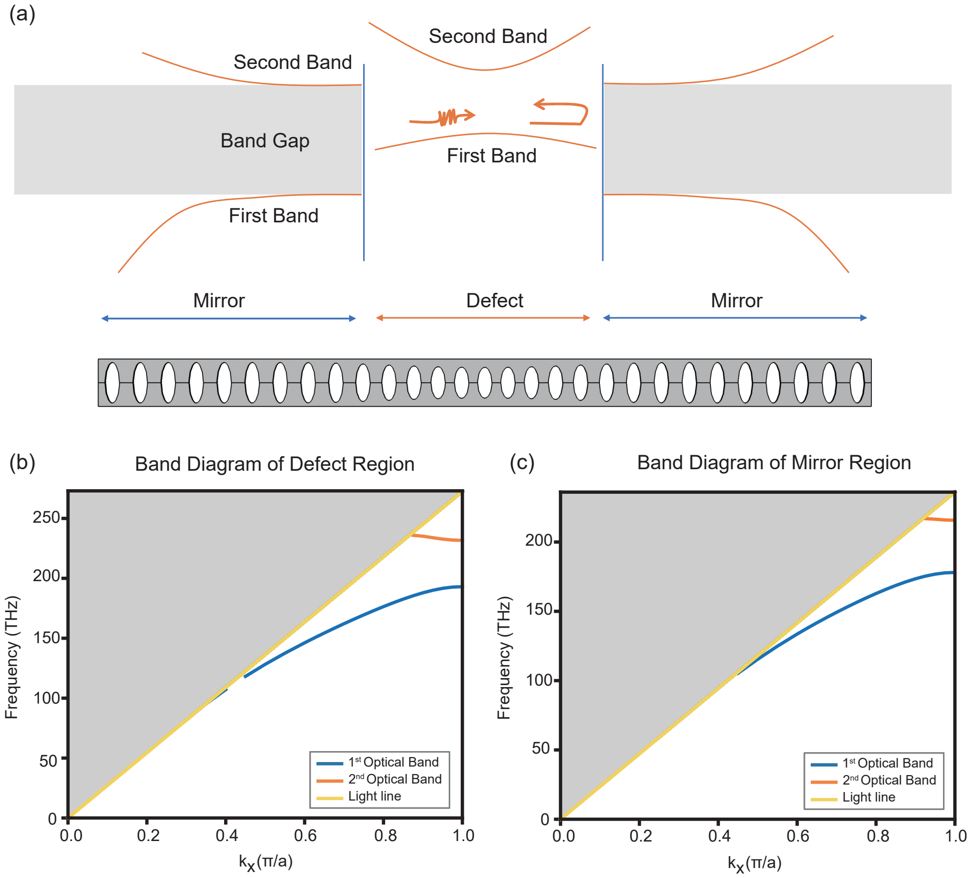

Figure 3.5: (a) The spatial geometry arrangement and the corresponding band structure for the nanobeam. (b) and (c) The band structure of the unit cells designed for the defect and mirror regions, respectively.

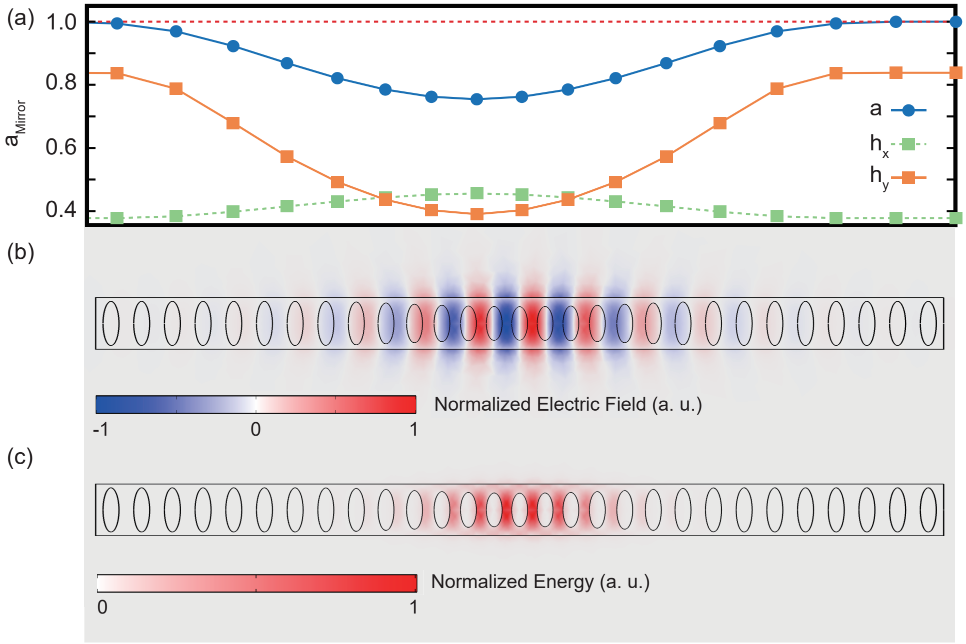

Figure 3.6: (a) The example of parameters transition from the mirror region to the defect region. (b) The geometry and the distribution of the y component of the electromagnetic field of the optimized nanobeam. (c) The energy distribution of the nanobeam. Figure (a) cited form [10].

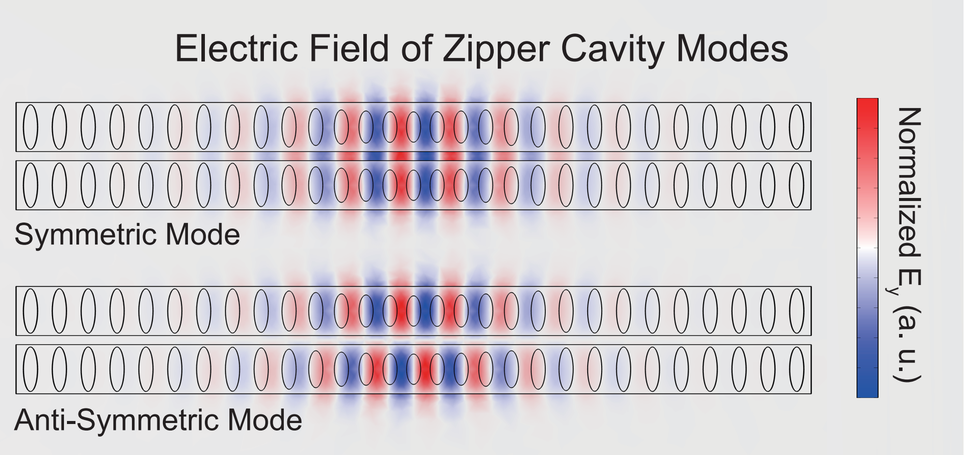

Figure 3.7: The electric field in the y direction (in-plane and perpendicular to the direction of the beam) of the symmetry (a) and anti-symmetry mode (b).

When two nanobeams are put close to each other, the original electromagnetic field of each nanobeam is coupled to the other [45]. The electromagnetic field will redistribute and the mode splits into symmetry and anti-symmetry ones. Therefore, a new optical cavity is constructed in this way and it's called a zipper cavity [9]. As we already have a well-designed nanobeam, we can make a zipper cavity by putting two nanobeams together parallelly in the x-y plane. The reason for doing this is that the optical property of the zipper cavity can be easily modified by changing the gap between the two nanobeams [45]. To study the electromagnetic field of the zipper cavity, we conduct the two simulations.

Firstly, the distance between two nanobeams is set as 100 nm and we simulate the electromagnetic field distribution of it. The result is shown in Fig. 3.7. Notably, for the symmetric mode, a significant proportion of the electromagnetic field is distributed inside the gap between two nanobeams, while for the anti-symmetric mode, there is nearly no field in the gap between them. The eigenfrequencies of these two modes are not degenerated. The eigenfrequency of the symmetry mode is lower than the original eigenmode frequency of the nanobeam, while the one of the anti-symmetry mode is higher.

Then, we simulate the zipper cavities with different gap distances between two nanobeams that construct it. The wavelengths of the eigenmodes of the symmetric and anti-symmetric modes change with different internal gap distances. The plot is shown in Fig. 3.8. Intriguingly, the changes in the wavelengths of two different eigenmodes are not the same. While the wavelengths of the anti-symmetric eigenmodes remain relatively stable, the wavelengths of symmetric eigenmodes change significantly, especially with a small distance. This is an ideal property as it shows high wavelength flexibility. The reason for different wavelength shifts of these two modes is caused by the different concentrations of

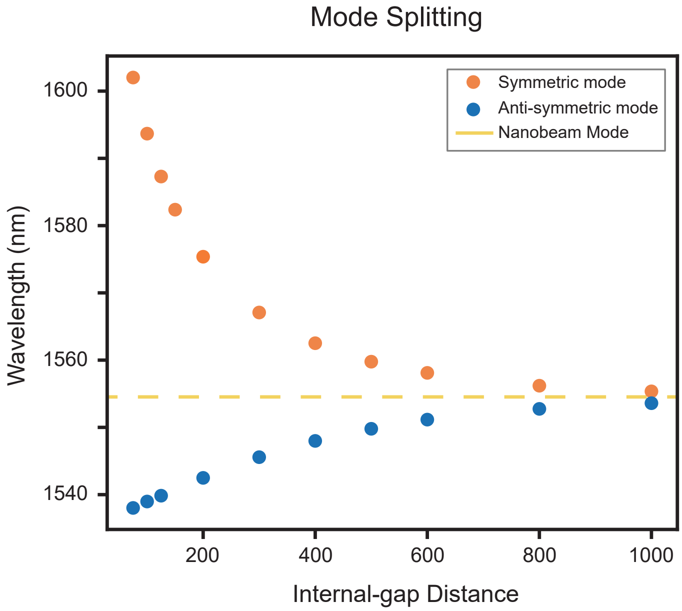

Figure 3.8: The change of the symmetry and anti-symmetry mode with different inter-beam gap distances.

the electromagnetic field inside the gap, which leads to a difference in the second-order self-coupling [13, 35, 45]. In addition, the eigenfrequencies of both modes converge to the eigenfrequency of nanobeam eigenmode with increasing distance. This is because that the coupling between two beams becomes weaker with a large internal gap distance and the mode splitting decreases.

By analyzing the change of these two zipper cavity modes, two conclusions are summarized to instruct our design of the zipper cavity. Firstly, to realize high wavelength tunability, the symmetric mode should be used as the target mode. Secondly, as the wavelength is more sensitive to the change of the gap when the gap distance is small, a small value is chosen when designing the zipper cavity. Therefore, considering the fabrication difficulty for tiny features, the gap distance is set to be 100 nanometers.

Therefore, from now on, we will focus on the symmetric mode of the zipper cavity. Some additional work is conducted to optimize the performance of the zipper cavity. While the wavelength of the symmetric mode is longer than the wavelength of the nanobeam, which means it's longer than our target wavelength of 1550 nm, we modified the structure of nanobeams that constructed the zipper cavity and the modified wavelength of the symmetric mode of the zipper cavity is 1550 nm when the gap distance is 100 nm. We also optimize the quality factor of the zipper cavity and the optimal quality factor we get is 1.47×10^7.

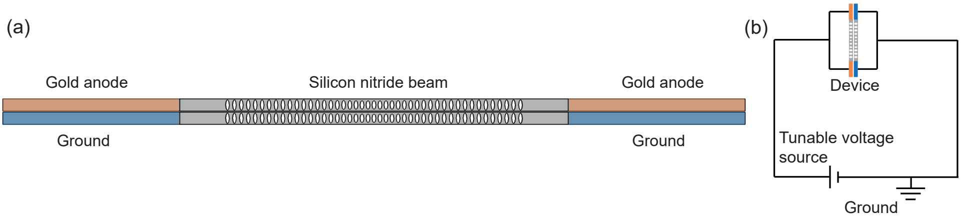

Figure 3.9: (a) The design of the zipper cavity with deposited electrodes. (b) The corresponding equivalent circuit of the device including external voltage source.

3.4. ELECTROSTATIC FORCE

Until now, we demonstrated a zipper cavity whose wavelength of the eigenmodes can be modified by changing the internal gap distance. In this section, we evaluate the feasibility of changing the gap distance by electrostatic forces. We first introduce how we set up the model for the electrostatic force simulation and estimate the magnitude of the deformation by the Young's modulus. Then we conduct the electrostatic force simulation and get the deformation field from it. We evaluate the change in the magnitude of the deformation with different voltages applied to it. Finally, we estimate the wavelength shift induced by the deformation.

The most intrinsic way to modify the gap distance of the zipper cavity is by the electrostatic force, which allows us to apply the force on the micrometer scale device. The model we used to simulate the electrostatic force is shown in Fig. 3.9 (a), which is based on the work of R. Perahia et al [34]. The length of the original zipper cavity is extended for 20 um and both ends are fixed. On both sides of it, gold electrodes with lengths of 16 um are put on the top of the silicon nitride nanobeams. The thickness of the electrodes is 100 nm. The voltages applied on the upper gold electrodes are set to be the same, and the magnitude of the voltage is set to be V_{dc}, while the lower two electrodes are set to be grounded. The corresponding equivalent circuit for this setting is shown in Fig. 3.9 (b). According to the electrostatics, an attractive force will be generated when there is a voltage difference between two plates of the capacitor. This force will induce a deformation of the zipper cavity and reduce the gap distance.

Before the simulation, we first estimate the deformation induced by the electrostatic force to check if our model is reasonable. The force applied to the nanobeam can be calculated by electrostatics. According to the theory section, the electrostatic force can be calculated by equation 2.35. The magnitude of the force is decided by the permittivity, plate area of the capacitor, voltage, and distance between two electrodes. For our device, the dielectric medium between the capacitor plates is air, whose permittivity is the vacuum permittivity. The area of the capacitor plates is the cross-section area of the gold electrodes in the z-x plane, which can be obtained by the production of the length and thickness of the electrodes. The voltage is set to be 10 volts, which is a value that most of the voltage sources can support. The distance between two plates is the same as the distance between two nanobeams. Substituting the parameters of our device to the equation, the total force provided by two capacitors on both ends is estimated to be 203 nanonewton.

Then, we estimate the deformation induced by this force. In the elastic region, the relation between the force and the deformation can be written as:

$$F = ExA \tag{3.4}$$

Where E is the Young's modulus of the material, A is the cross-section area, and x is the deformation. With the electrostatic force calculated above, the deformation perpendicular to the beam is estimated to be about 22.7 nanometers, which is a relatively reasonable value that is neither too large that collapse the beam nor too small to influence the gap distance. Nevertheless, the exact deformation still needs to be simulated to get a result that is more consistent with the real experience.

As we show by the estimation that the model will give a reasonable deformation, we can conduct simulations to obtain an accurate deformation field induced by the electrostatic force. Firstly, the deformation of the whole beam was simulated with a voltage from 0 to 12 volts. The result is plotted in Fig. 3.10. The distribution of the displacement from the original position induced by the electrostatic force is shown in Fig. 3.10 (a). As both ends of the beam are fixed, the displacement is negligible close to these regions and reaches a maximum at the middle point. In addition, the deformation of two nanobeams is anti-symmetric as the electrostatic force applied to them is anti-symmetric. The relation between the magnitude of the deformation and the voltage is demonstrated in Fig. 3.10 (b). The deformation of the beam is evaluated by the displacement of the middle point of the beam. The reason for choosing this value is that the concentration of the electromagnetic field meets the maximum in this region, thus the deformation around this region is more influential to the frequency shift. Notably, the increase of the deformation gets more significant as the voltage gets higher, which is caused by the electrostatic force's quadratic dependence on the voltage.

As we show the maximum deformation of the zipper cavity is about 16 nm for each nanobeam, which means a decrease of 32 nm in the total gap width, we then simulate wavelength shift corresponding this gap change. We simulate the wavelengths of the symmetric eigenmodes with the gap distance from 100nm, e.g. the original designed value, to 70nm. The result is shown in Fig. 3.10 (c). We can see that the wavelength of the symmetric eigenmode can be tuned up to 10 nanometers.

3.5. OPTOMECHANICAL COUPLING

Until now, we have shown that the deformation of the zipper cavity can be modified by the voltage on it. In this section, we combine the electrostatic force simulation and the optics simulation to show the wavelength shift induced by the deformation. After that, with the deformation field and the electromagnetic field obtained from the simulation,

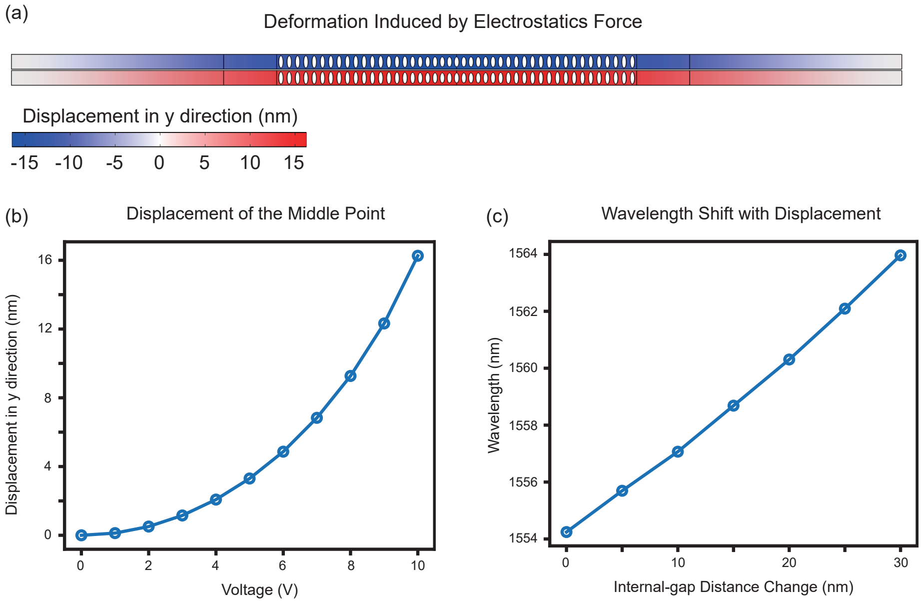

Figure 3.10: (a) The distribution of the deformation over the zipper cavity induced by the electrostatic force with a voltage of 10 volts. (b) The deformation of the zipper cavity. Values are taken from the displacement of the center point of each nanobeam. (c) The shift of the wavelength with decreased gap distance. The range of the distance is decided by the magnitude of the deformation of the electrostatic force simulation result.

we calculate the optomechanical coupling factor to evaluate the wavelength tunability of our device.

In the combined simulation, the electrostatic force is first applied to simulate the deformation of the structure. After that, the deformed structure is used as the dielectric geometry for the electromagnetic field simulation to get the wavelengths of the eigenmodes of the structure. Fig. 3.11 shows the change of the symmetric eigenmode wavelength of the deformed device with different voltages applied to it. We can see that the shift in wavelength has a similar tendency to the change of the middle point position. According to the estimation, the wavelength shift is nearly linear with small deformation. In addition, the deformation is nearly quadratically dependent on the voltage. Therefore, it's consistent with the expectation that the wavelength should also be nearly quadratically dependent on the voltage. With 12 volts of voltage, we got the highest detuning of 21 nanometers.

As introduced in the theory chapter, the factor which evaluates optical frequency shift per displacement is called the optomechanical coupling factor. According to the moving dielectric boundary theory, the relation between the G factor and the deformation field can be described by the equation 2.54. From the equation, the optomechanical coupling factor is decided by the deformation and the electromagnetic field distribution. As we realized both the simulation of the electrostatic force and the electromagnetic field,

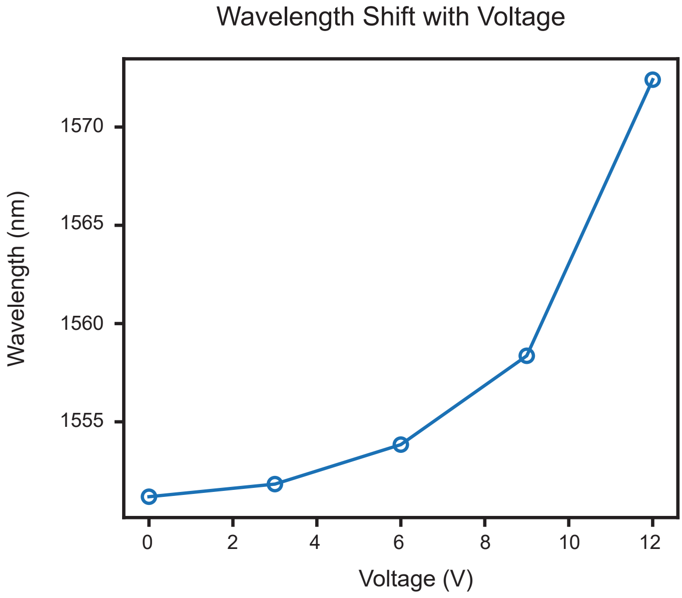

Figure 3.11: The change of the wavelength of the symmetric mode with different voltage applied to it.

it's possible to use the result of these two simulations to calculate the optomechanical coupling factor. The normalized deformation field can be derived from the electrostatic force simulation, while the electromagnetic field and electric displacement can be obtained from the electromagnetics simulation. Substituting the values obtained from the simulation to this formula, we can get the G factor for 89 GHz/nm, or 0.69nm/nm, which is comparable with the result achieved by previous works [34]. The G factor also indicates that we will have a wavelength change for 0.69 nm with the gap distance change of 1 nm, which is also close to the result of our simulation.

3.6. OPTICAL RESPONSE

Until now, we have the complete design of our wavelength tunable cavity. In this section, we focus on the simulation of the optical response of our cavity with an input source. First, we introduce the model and the input source we used in the simulation. Then, we conduct the simulation and demonstrate the distribution of the electromagnetic field distribution with different input frequencies. Finally, the theoretical and simulated reflection probability is evaluated with different waveguide-cavity coupling distances.

The model used for the response simulation is shown in Fig. 3.12 (a). The light is inputted from the right side of the simulation area, propagates through the waveguide, and is evanescently coupled into the cavity. In addition, in the real experiment, the reflection spectrum will be measured considering the current test setup. Therefore, the pattern of the mirror region which is used to prevent the light from going through is also

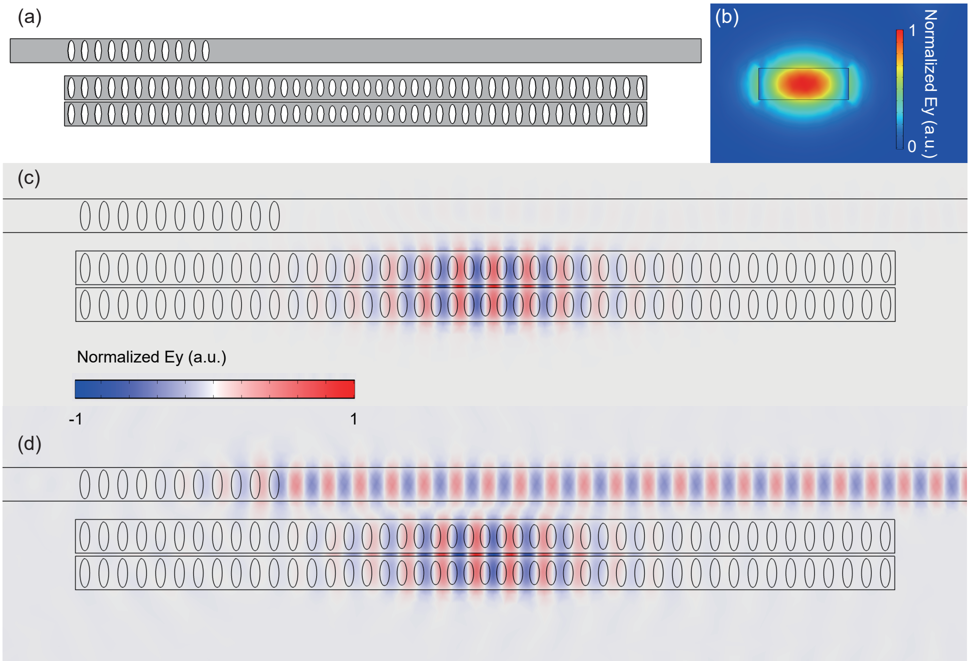

Figure 3.12: (a) The scheme of the optical response simulation. The structure contains the zipper cavity and input waveguide. (b) The electric field distribution of the TE_{00} mode of the input waveguide. (c) and (d) The distribution of the electric field with on-resonance and off-resonance (20 GHz detuning) input.

patterned on the left side of the waveguide. In this way, all the light that is not coupled into the cavity or is coupled back from the cavity will all be reflected to the right port while nothing will go to the left port.

In addition, the initial value of the distance between the waveguide and the cavity is set to be 500 nm. In the simulation, we want to be able to control the intrinsic loss rate κ_{in} and the external coupling rate κ_{ex}. While we already have the designed cavity, the intrinsic loss rate is already fixed. However, we can still change the external coupling rate by changing the distance between the waveguide and the cavity. Therefore, by simulating the optical response of the models with different waveguide-cavity distances, we can get the response of the devices with different ratios between the intrinsic loss rate κ_{in} and the external coupling rate κ_{ex}.

Another preparation work for the response simulation is to evaluate waveguide mode which is used as the input signal in the simulation. As the width of the waveguide is much less than the threshold of the TE_{01} mode, the only mode that the cavity can support is the TE_{00} mode. Fig. 3.12 (b) shows the simulation result of the electric field distribution of this mode. The damping rate of the mode is 2.4×10^{-9} dB/m, which means less than 10^{-13}dB damping in our system scale (100 um) and it's negligible. Therefore, with the model we set and the input signal we found, we can simulate the optical response of our cavity.

We first evaluate the electromagnetic field distribution of the system. Fig. 3.12 (c) and (d) show the electric field distribution with on-resonance and off-resonance input, respectively. We can see that with on-resonance input, which means the input signal is exactly at the eigenfrequency of the cavity. We can see that most of the light field are coupled into the cavity while the residual in the waveguide is neglectable, which means a low reflection probability. However, when the input frequency has a 20 GHz detuning, we can see a significant decrease in the field inside the cavity while the signal in the waveguide is dramatically enhanced. This means only a small fraction of the light at this frequency is coupled into the cavity, and this leads to a high reflection probability.

Then we evaluate the theoretical reflection probability with different ratios between the intrinsic loss κ_{in} rate and the external coupling rate κ_{ex}. The theoretical result is based on equation 2.58. The result is shown in Fig. 3.13 (a). We can see that the minimum and the linewidth of the reflection dip are determined by the intrinsic loss rate and external coupling rate. When the intrinsic loss rate equals the external coupling rate, the minimum of the dip reaches the minimum point, e.g. zero reflection, thus this coupling ratio is called critical coupling which indicates the coupling with the best performance and highest efficiency. With increasing external coupling rate, the line width of the dip will get broader, which means that the photons with larger detuning also have a chance to be coupled into the cavity. In addition, the minimum of the dip will become larger, which is caused by the increasing probability of the photons inside the cavity being coupled back to the waveguide. On the other hand, with a smaller external coupling rate compared to the internal losing rate, the line width will become narrower, which indicates a smaller probability for the detuned photon to be coupled into the cavity. Simultaneously, the on-resonance photon also has a smaller probability of being coupled into the cavity, which leads to a larger minimum value of the dip. Therefore, considering that we want to use it for a spectrometer, there is a trade-off between the efficiency (the minimum of the reflection) and the resolution (the line width). As in real situations, a high sensitivity is desired in multiple fields, which means the detection efficiency should be considered more. Therefore, the ideal coupling strength for our device should be the one at the critical coupling point.

Finally, we conduct the simulation of the cavity with different waveguide-cavity distances. The result is shown in Fig. 3.13 (b), and it's consistent with the theoretical prediction. We can see a clear change in the minimum and the line width of the response signal with different waveguide distances. With a near distance at 300nm, the dip is significantly broadened, while oppositely, the dip gets narrow and shallow at 900nm nm, which is a relatively big distance. The minimum of the dip appears at 600nm, and with a slightly smaller or larger distance (500 or 700nm), a significant change in depth and line width can be observed. Therefore, we can conclude that with a waveguide distance of 600nm, we can have a critical coupling between the waveguide and the cavity. When the distance is shorter, the cavity is over-coupled. Oppositely, with a longer distance, the cavity is under-coupled [4].

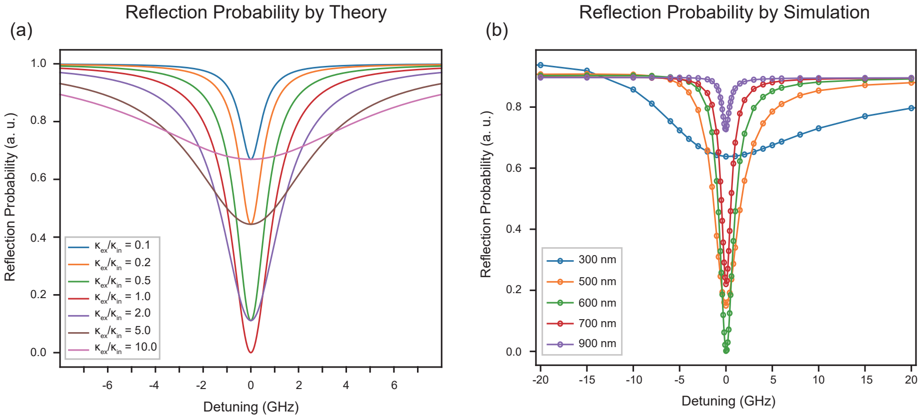

Figure 3.13: (a) The reflection probability with different ratios between external coupling rate and intrinsic loss rate derived from the input-output theory. (b) Simulation of the reflection probability with different distances between the waveguide and cavity.

4

EXPERIMENT

Through FEM simulation, we get our design of the zipper cavity which we expect to have an ideal optical response. After fabrication, we get a chip with multiple devices that have different geometry parameters for each device. Then, the devices are tested using the reflection spectrum. The aims of the experiment are mainly two things. Firstly, we need to check the consistency of the actual response and our simulation and design. Secondly, some parameters, such as the external coupling strength, are difficult to get from the theory and simulation. We hope to figure out an ideal geometry parameter for it by attempting different designs.

In this chapter, we first introduce the devices we used in our experiment in section 4.1. The devices are fabricated with different geometry parameters which allows us to compare them and analyze the influence of each parameter. After that, in section 4.2, we introduce the setup for the reflection spectrum, which will be mainly used in the following experiments. Then, we demonstrate the reflection spectrum we get and introduce how we extract the resonance wavelength and the total loss rate of the cavity from it in section 4.3. Finally, we analyze three sets of devices. The intrinsic loss rate and the external coupling rate are evaluated by comparing devices with different waveguide-cavity gap distances in section 4.4. In section 4.5, the tunability of resonance wavelength is investigated by studying devices with different internal gap distances. We also study devices with different hole sizes to prove that they can work in different wavelength ranges in section 4.6.

4.1. DEVICES

The devices are fabricated based on the simulation result. In this section, we introduce the structure of the devices. The meaning of each geometry parameter is also introduced. The geometry parameters are varied from device to device for further investigation of the influence of them.

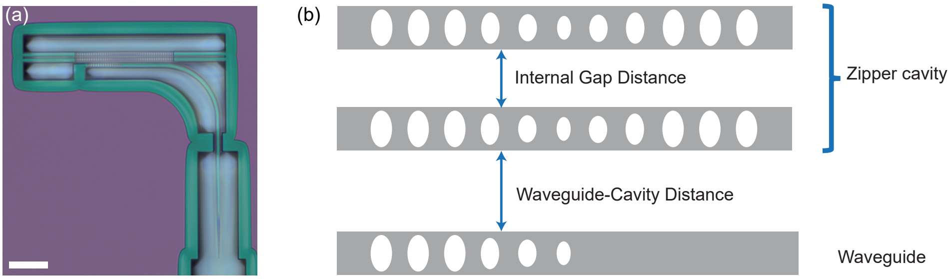

Figure 4.1: The geometry of the devices. (a) The picture of the device after fabrication. The scale bar is 10 um. (b) The sketch of the sample structure with geometry parameters marked on it.

The geometry of the fabricated device is shown in Fig. 4.1 (a). Following the simulation and the design, the device is constructed by a zipper cavity and a coupling waveguide with a tapered tail which is used for coupling to the input fiber. The size of the holes patterned on the zipper cavity is decided by the simulation result (see Chapter 3). Besides, two more parameters decide the geometry of the samples, which is demonstrated in Fig. 4.1 (b). The distance between the two nanobeams that constitute the zipper cavity is called the internal gap distance. The distance between the zipper cavity and the coupling waveguide is called the waveguide-cavity distance. The combination of these parameters decided the geometry of the device.

To study the influence of each geometry parameter, these parameters are varied from device to device. Firstly, according to the input-output theory introduced in Chapter 2 and the simulation of the reflection response shown in Chapter 3, the reflection response of the device is decided by the external coupling rate, which can be changed by the waveguide-cavity distance. Therefore, the waveguide-cavity distance is varied from 200 nm to 800 nm with a 100 nm difference between each of them. In addition, as discussed in the simulation of the zipper cavity resonance wavelength in Chapter 3, the resonance wavelength of the cavity is decided by the internal gap distance. To prove that the resonance of the cavity can be changed, we vary the internal gap distance from 200 nm to 400 nm with a difference of 50 nm between each of them. Finally, based on the photonic crystal theory introduced in Chapter 2, the resonance of the cavity is decided by the widths of materials with different refraction indices. For our devices, the widths of the air and the silicon nitride are decided by the size of the holes patterned on the nanobeams. Therefore, besides the devices with the hole sizes that are obtained from the simulation, we also fabricate devices whose hole sizes are 10 nm and 20 nm larger. Therefore, we have 7 different waveguide-cavity distances, 5 different internal-gap distances, and 3 different hole sizes. Combining these three sets of parameters, we have $7 \times 5 \times 3 = 105$ devices.

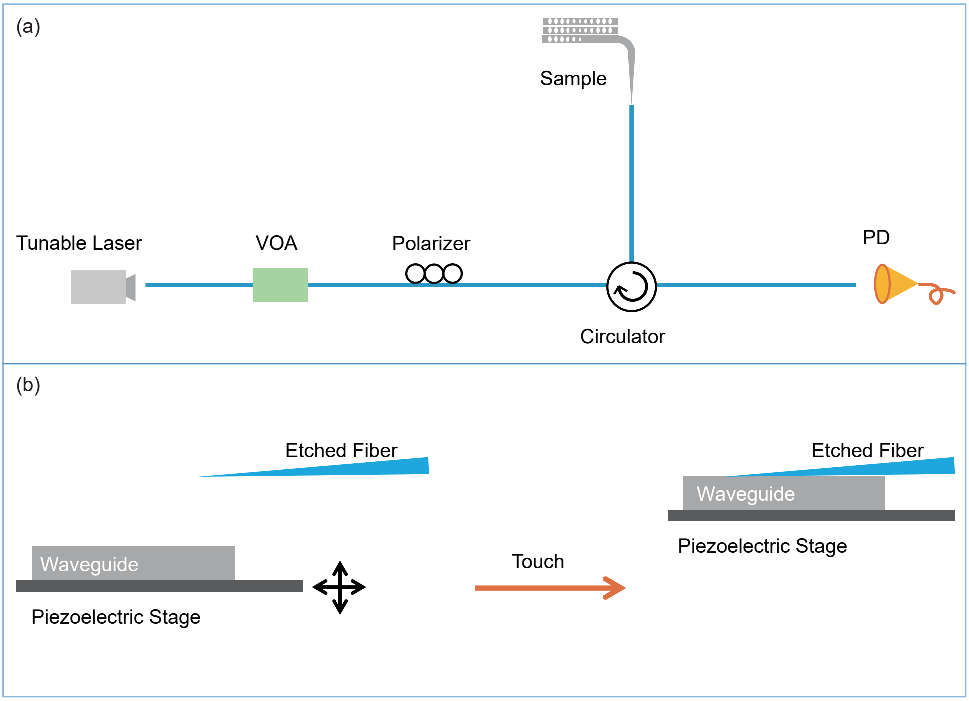

Figure 4.2: (a) The scheme of the test setup for the reflection spectrum. (b) The sketch of the method to couple the etched fiber to the waveguide.

4.2. EXPERIMENT SETUP

In our experiment, the reflection spectrum is used to investigate our cavity, not only because it can easily give us the internal and external coupling rate through the input-output theory, but also because our current test setup in the lab is suitable for this measurement. In this section, we will introduce the experiment setup for the reflection spectrum.

The sketch of the reflection experiment setup is shown in Fig. 4.2 (a). The laser is generated by a tunable laser source (Suntech). Using the variable optical attenuator (VOA), the intensity of the laser can be modified. The TE mode is realized by the polarizer and sent into the sample through the oscillator. After interacting with our cavity, certain proportions of the light will reflect according to its wavelength. The light will be sent to the circulator and directed to the photon detector (PD), through which the intensity of the reflection light will be recorded. As the laser source is tunable, by tuning the input signal and recording the corresponding reflection intensity, we can get the relation between the reflection and the wavelength, which is the reflection spectrum that we want.

An additional point to claim is the method we use to couple the fiber of the test setup and our device in our on-chip measurement. The sketch of the connection between the

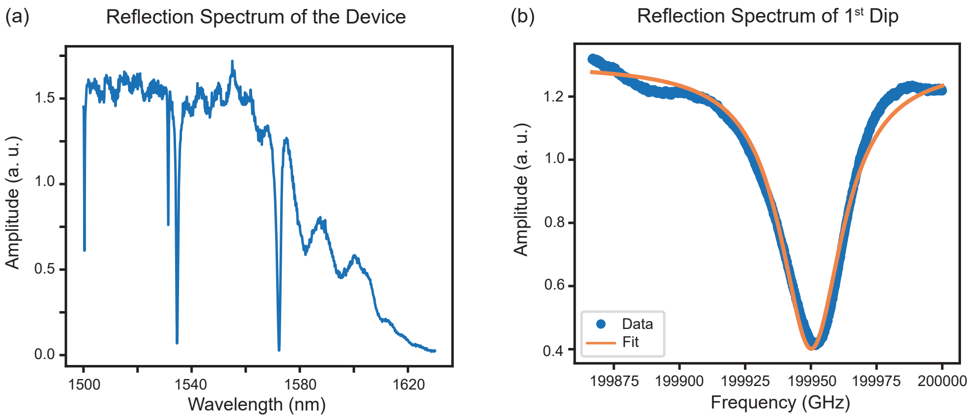

Figure 4.3: The reflection spectrum of the device. (a) The coarse scan over a large wavelength range. Four obvious dips appear on the spectrum. (b) The zoom-in of the dip and the fitting by Lorentz distribution.

fiber and the device waveguide is shown in Fig. 4.2 (b). The end of the fiber in the input arm of our test setup is connected to an etched fiber, which is etched by the HF to a tapered shape. In this way, the fiber can evanescently couple the light to other systems through touching it. The device is placed on a piezoelectric stage which can move the device with the accuracy of micrometers. In this way, we can move our device and touch the fiber, which allows us to couple the light into our cavity.

4.3. REFLECTION SPECTRUM

Using our experiment setup, we can get the reflection spectrum of our device. In addition, in the design and simulation section, we introduced that we could use the reflection response of our device to characterize our device (for example, to get the coupling rate). Here, in detail, we will discuss the result of the reflection measurement and how we use it to evaluate the performance of our device.

A typical reflection spectrum of our device is shown in Fig 4.3 (a). There are four obvious dips in the spectrum that indicate low reflection probabilities around them. According to our simulation and previous works, the first-order eigenmodes have the highest eigenfrequencies, which also means the shortest wavelength, while the higher-order modes have longer wavelengths [9]. In addition, for the eigenmodes with the same order, the anti-symmetric mode has a shorter wavelength. We also checked that there are no additional dips in the shorter wavelength range. Therefore, we can conclude that the dips in the spectrum, ranging from shorter to longer wavelengths, correspond to the first-order anti-symmetric mode, first-order symmetric mode, second-order anti-symmetric mode, and second-order symmetric mode, respectively.

To get more insight into the device's reflection response and extract more information about our cavity through it, we conduct zoom-in fine scans for each dip. The result is shown in Fig. 4.3 (b). To analyze the reflection dip, let's first recall the input-output theory. The reflection probability can be written as:

$$|R|^2 = 1 - \frac{\kappa_{\text{in}}\kappa_{\text{ex}}}{(\frac{\kappa_{\text{in}}+\kappa_{\text{ex}}}{2})^2 + \Delta^2}. \tag{4.1}$$

However, in our situation, the test setup doesn't contain the reference light path, which makes it impossible to get the reflection probability. The reflection spectrum we got is the unnormalized reflected intensity which is decided by both the reflection probability and the laser intensity distribution over different wavelengths. In addition, other factors influence the reflection spectrum, for example, the background signal, the laser fluctuation, and other noises. Therefore, considering all of these factors, the function we used to fit the curve is:

$$I_{\text{R}} = \text{offset} - \frac{a}{(\frac{\kappa_{\text{in}}+\kappa_{\text{ex}}}{2})^2 + \Delta^2}, \tag{4.2}$$

where offset and a refer to the effective influence of all other factors. We use the I_{R} to replace $|R|^2$ in order to emphasize that the things we get are the reflection intensities instead of normalized reflection probabilities. Although the offset and the scale a are ambiguous and impossible to get, we can see that the reflection intensity is in the form of Lorentz distribution, which means that the full width at half maximum (FWHM), or we say the linewidth of it, is only dependent on the sum of the intrinsic loss rate and external coupling rate with the relation $\text{FWHM} = \kappa_{\text{in}} + \kappa_{\text{ex}}$. Therefore, through this Lorentz fitting, we can get the total loss rate. Note that the function is written based on frequency, but our reflection spectrum is based on wavelength. Thus, we need to first convert the result into frequency and then conduct the fitting.

In addition, the quality factor, which evaluates the ability of the cavity to confine the energy, is also an important factor for us to characterize the performance of our cavity. Based on its definition, the quality factor Q of a cavity can be written as:

$$Q = \frac{W_{\text{cavity}}}{W_{\text{loss}}} = \frac{\hbar\omega_{\text{cavity}}}{\hbar\omega_{\text{loss}}} = \frac{\omega_{\text{cavity}}}{\kappa_{\text{in}} + \kappa_{\text{ex}}}. \tag{4.3}$$

Therefore, with the total loss rate, e.g. the linewidth we get from the fitting, we can also get the quality factor of our cavity.

4.4. EVALUATION OF COUPLING RATE

As mentioned before, it's relatively difficult to get the ideal waveguide-cavity distance which gives us the external coupling rate that leads to the critical coupling. Therefore, in this section, we measure the devices with different waveguide-cavity distances to find the best-performed one among them by experiment.

Firstly, we need to decide which devices we need to measure. To compare the external coupling rate, we need to vary it while keeping other parameters fixed. According to the expression of the reflection spectrum, we can find that the external coupling rate, intrinsic loss rate, and resonance frequency all influence the final spectrum we get. Therefore, while changing the external coupling rate, we want to fix the intrinsic loss rate and the resonance wavelength. Since our waveguide is evanescently coupled to the cavity, the external coupling rate is most sensitive to the waveguide-cavity gap distance. The intrinsic loss rate is mainly decided by the fluctuation in the fabrication. In addition, as discussed in the design section, for a zipper cavity constructed by certain nanobeams, the resonance frequency mainly depends on the internal gap distance. Therefore, we choose 7 samples with different waveguide-cavity gap distances and the same internal gap distance and compare them. The waveguide-cavity gap distance is set to be from 200 to 800 nm with a 100 nm increase for each device, and the internal gap distance of these 7 devices is fixed to be 200 nm. In addition, we showed by the simulation that the symmetric mode is more sensitive to the change of the internal gap distance, which means it has better tunability in the resonance wavelength. Therefore, our study will focus on the symmetric mode, e.g., the second dip in our reflection spectrum.

In addition another fitting equation is needed to extract the external coupling rate from the FWHM we get. To investigate the change of the coupling rate with different waveguide-cavity distances, we compare the FWHMs over these devices, which gives us information about the total loss rate. However, we cannot figure out the intrinsic loss rate and the external coupling rate separately. Therefore, we need to further investigate the result. As the intrinsic loss rate is relatively fixed, we can suppose it's identical over these samples and only the external coupling rate is different over samples. In addition, as the light is evanescently coupled to the cavity, the coupling strength exponentially decays with the increasing distance [7]. Therefore, the relation between the total loss rate and the waveguide-cavity gap distance d_{WC} can be written as:

$$\mathrm{FWHM} = \kappa_{\mathrm{in}} + \kappa_{\mathrm{ex,200nm}} e^{-(d_{\mathrm{WG}}-200nm)/d_0}, \tag{4.4}$$

where d_0 is the decay length of the coupling strength. We can use this function to fit the FWHMs we get. Through this way, we can get the κ_{ex} for a 200 nm waveguide-cavity distance and the κ_{in} and d_0 for all the devices. The external coupling rate for other devices can be calculated by the calculated by the function with their waveguide-cavity gap distance.

With the methods mentioned above, we conduct the experiment and analyze the reflection spectrum we get. The result is demonstrated in Fig. 4.4. The FWHM of the reflection dip decreases with the increase of the waveguide-cavity gap, which is caused by decreased external coupling rates. In addition, with a large waveguide-cavity distance, the change in the total loss rate becomes smaller, which indicates an exponential decay of the external coupling rate instead of a linear change. The fitted result is shown by the orange line in Fig. 4.4. The intrinsic loss rate obtained by the fitting is 12.43 GHz and the external coupling rate at 200 nm is 27.35 GHz. The fixed intrinsic loss rate is shown

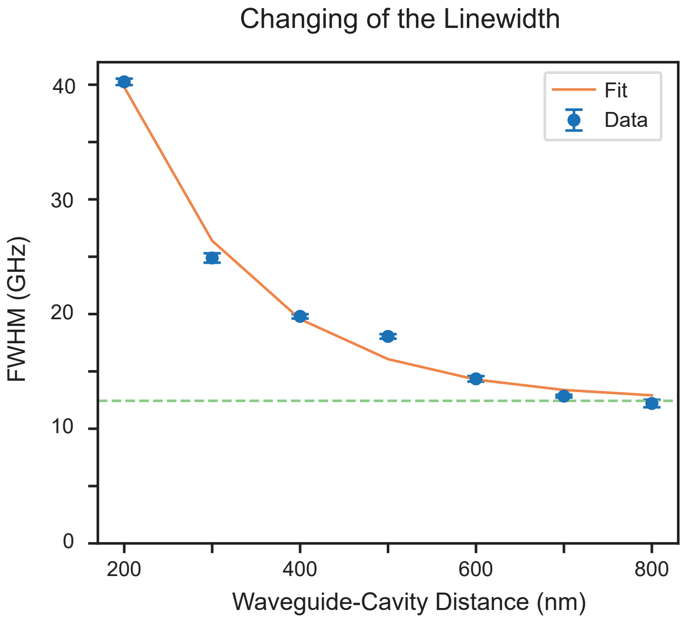

Figure 4.4: The changing of the FWHM with different waveguide-cavity distance. The dashed horizontal line refers to the intrinsic loss rate.

by the green dashed line in Fig. 4.4. We can see that the FWHMs converge to that line with increasing waveguide-cavity distance, which is caused by the fact that the external coupling rate decays with the distance while the internal loss remains the same. In addition, as we mentioned in the simulation section, we want to find a distance that gives the same external coupling rate and the internal losing rate which leads to the critical coupling. Through this fitting result, we can find that when the waveguide-cavity gap distance is 400 nm, the external coupling rate is closest to the intrinsic loss rate, which leads to a critical coupling. From now on, we will evaluate the devices with this best-performed parameter.

4.5. SHIFT OF THE RESONANCE

Now we have found the waveguide-cavity distance for the critical coupling. Another goal for our measurement is to prove the tunability of the resonance of our device. In this section, we measure the devices with different internal gap distances to show the wavelength tunability of them.

Currently, we haven't finished the fabrication of the devices with electrodes that make it possible to tune their resonance. Therefore, the only thing we can do now is to compare the wavelengths of devices with different internal gap distances. If the resonance wavelengths change over the devices with different internal gap distances, we can say

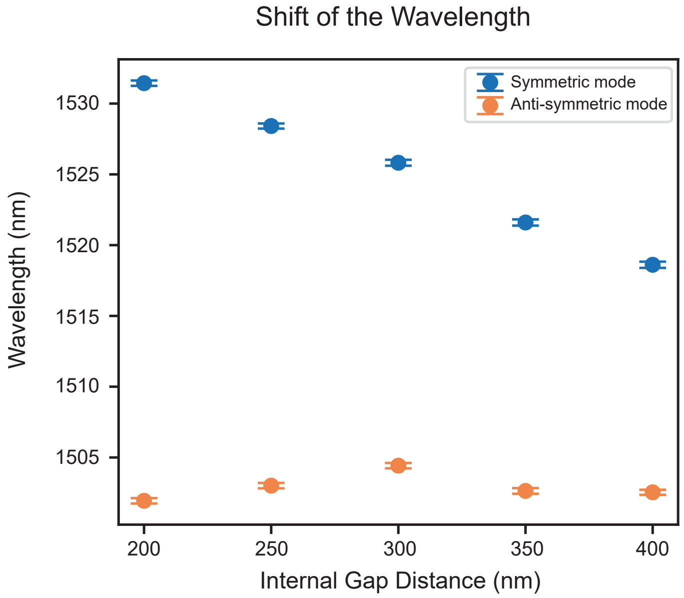

Figure 4.5: The resonance wavelengths of devices with different internal gap distances. We can see the wavelengths of symmetric modes decrease with increasing internal gap distance, while the wavelengths of the anti-symmetric modes remain nearly the same.

that we will be able to tune the resonance wavelength of the cavity once we can apply electrostatic force on it and change the internal gap distance. To show the changing of the resonance wavelength we measured the devices with fixed waveguide-cavity gap distances of 400 nm and different internal gap distances from 200 nm to 400 nm with the increase of 50 nm for each device.

The result is shown in Fig. 4.5. Consistent with what we showed in the simulation, the wavelengths of the symmetric modes decrease with the increasing internal gap distance, while the wavelengths of the anti-symmetric modes don't have an obvious shift. The wavelengths of the symmetric modes change from 1531.44 nm to 1518.61 nm, which has a shift of 12.83 nm. The shift of 12.83 nm in the resonance wavelength is consistent with our simulation result, which changes for 13 nm when the internal gap distance changes from 200 nm to 400 nm. The shift of 12.83 nm is not a big change. The reason is that, as we showed in the simulation, the shift of the resonance is less significant with large start and end internal gap distances. The wavelength shift of the device with the internal-gap distance from 100 nm to 300 nm is nearly twice compared to the device whose gap changes from 200 nm to 400 nm. With optimized fabrication strategies, we expect to be able to fabricate devices with smaller internal gap distances, which will lead to a significant increase in the tunability of the resonance wavelength.

4.6. MODIFYING THE WAVELENGTH RANGE

Now we have shown the tunability of our devices, whose resonance wavelength can be changed from 1531.44 nm to 1518.61 nm by changing the internal gap distance. In this section, we measure devices with different hole sizes to show that we can modify the range in which the wavelength is tunable by modifying their geometry.

To further evaluate the performance of our device, we show that we can modify the tunable range of the wavelength. This requires us to change the resonance wavelength while keeping the internal gap fixed. Based on the photonic crystal theory introduced in the second chapter, the resonance wavelength can be changed by changing the size of different dielectric materials. The reason for this phenomenon can be simply explained by the equation 2.28, which is:

$$n_1 d_1 + n_2 d_2 = \frac{\lambda}{2} \tag{4.5}$$

Suppose that n_1 denotes the refractive index for air and n_2 for the silicon nitride. With an increase in d_1 and a decrease in d_2 with the same amount, we will expect a shorter resonance wavelength. By changing the sizes of the air holes patterned on the cavity, we can change the size of the air and the silicon nitride and further change the resonance wavelength. Therefore, in this experiment, three sets of devices were measured. Within each set, the air hole sizes and the waveguide-cavity distance are fixed. The internal gap of the cavity changes from 200 nm to 400 nm. For the first set of devices, the hole size is the same as the original design. For the other two sets, both the width and the height of the hole sizes are enlarged for 10 nm and 20 nm, respectively.

The resonance wavelengths of these three sets of devices are shown in Fig. 4.6. Within each set of devices, we can see a decrease in the wavelength with increasing gap distance, which is consistent with our previous measurement result. In addition, a clear shift of the wavelength range can be seen between different device sets. For the set with original hole sizes, the wavelength is tuned from 1531 nm to 1518 nm. For the other two sets, the wavelength shift range is from 1523 nm to 1509 when the hole size is 10 nm larger, and from 1513 nm to 1501 when the hole size is 20 nm larger. This result shows that the range in which the resonance wavelength is tunable can be modified simply by changing the geometry of our devices.

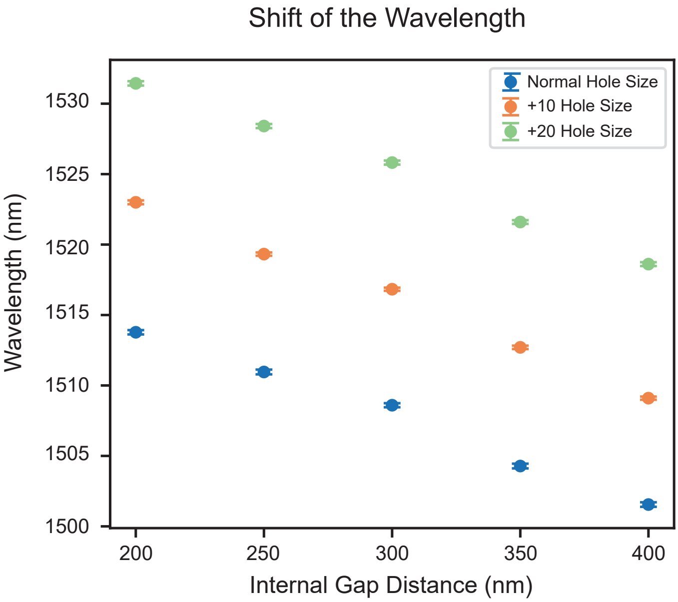

Figure 4.6: The wavelengths for devices with different hole sizes. We can see a significant shift between each set of devices.

5

CONCLUSION AND DISCUSSION

In this work, we designed a zipper cavity with tunable resonance wavelength in order to achieve an on-chip tunable spectrometer. The prototypes of the cavity were fabricated and the optical response of them were tested.

Based on FEM simulations and with the assistance of the simulator COMSOL, we designed the unit cells of the photonic crystals with a bandgap of 37 THz width around our target frequency of 193 THz. With transition functions, whose parameters were optimized through the Nelder–Mead algorithm, we designed a nanobeam cavity with a high quality factor. By putting two nanobeams together, we designed a zipper cavity whose resonance wavelength can be changed in a range of 49 nm by changing the internal gap distance. After that, we put gold electrodes on both ends of our cavity and simulated the deformation of it caused by the electrostatic force. The change in the gap distance induced by the electrostatic force was found to be more than 30 nm. Combining the electrostatic force simulation and the optical simulation, we show the resonance wavelength of the cavity can be tuned for 21 nm. The optomechanical coupling factor is also calculated to be 0.69 nm/nm. Finally, with an input source, the optical reflection response of the cavity was evaluated.

With the designed structure, the prototypes of the devices were fabricated. By comparing devices with different parameters, we figured out the intrinsic loss rate of the devices to be 12.43 GHz. We also showed the resonance wavelength of the devices can be changed for 12.83 nm with the internal gap distance changed from 200 nm to 400 nm. By changing the hole sizes of the devices, we demonstrated that the operation wavelength range can be modified. All these features proved that our cavity could serve as a high-resolution wavelength tunable filter, which is a key component for the on-chip spectrometer.

There are some previous works about the zipper cavity. The idea of using electrostatic force to tune the cavity, which is used in this project, was proposed by Teodoro Graziosi in this master thesis [18]. Based on his work, in this thesis, we further focus on the electromagnetic property of the cavity and the tunability of the optical modes. We optimized the features that are important for using it as a spectrometer such as the linewidth and the wavelength tunable range. These are also tested by measuring the prototypes of the cavity.

While the performances of the prototypes of our devices have been evaluated, there are still some problems to solve to optimize the performance of our zipper cavities. Firstly, the linewidth of the absorption dips for our device is about 28 GHz, which means a quality factor of 6.8 thousand and a resolution of 0.22 nm. This quality factor is still lower than our expectations. As this is the first chip successfully fabricated, we still need to optimize the fabrication process, through which we expect to minimize the fabrication fluctuations and have a higher quality factor, which will lead to a higher resolution.

Another problem is that the current wavelength tunable range is 12 nm with the gap distance changes from 200 nm to 400 nm. The tunable range is not broad enough and it's difficult to change the gap for 200 nm by electrostatic force. However, based on the simulation and previous works [45], we know that the resonance wavelength of the symmetric mode becomes more and more sensitive to the change of internal gap distance with a smaller internal gap distance. After the electrode deposition and the voltage applied to it, we can start with 200 nm or some slightly smaller initial value and further decrease the gap distance by the attractive electrostatic force. Based on the simulation, the wavelength is tuned for 13 nm with the gap distance decreasing from 400 nm to 200 nm. However, with the gap distance decrease from 200 nm to 75 nm, the wavelength will be tuned for more than 26 nm. Therefore, although the wavelength tunability is not ideal now, we expect a much larger tunable range after we are able to apply electrostatic force to it.

Besides solving these problems, we also plan to conduct some other work to realize a complete spectrometer. Firstly, we need to deposit electrodes on the cavities and wire-bound them to the printed circuit boards. This procedure allows us to apply electrostatic force on it. The force will cause the deformation and further enable us to tune the resonance wavelength of the cavity.

In addition, our current focus is on the zipper cavity which serves as the filter in our spectrometer. However, to achieve a complete spectrometer, we also need a detector to convert the photons to signals. To achieve an on-chip photon detector, we plan to use superconductor nanowire single-photon detectors (SNSPD). Previous works have already shown the feasibility of this method [41], and we also conducted simulations which show that we can achieve a photon absorption rate for more than 87% by this method.

ACKNOWLEDGEMENTS

Firstly, I would to thank my supervisor Professor Simon Gröblacher. Thanks for his direction and help in my project. Then, I would like to appreciate my group members. I learned lots of things from this group. Especially, thanks to Harmen, Xiong, and Jin. Thanks for their help in the project. Thanks to my committee members for their criticisms and suggestions. Also, I would like to thank all the teachers who gave me courses during my master learning.

Thanks to my friends. I have met various interesting people here and thanks a lot for your company during these two years. Also thanks to my old friends. Although we are in different countries, we are not separated. Thanks to my girlfriend. Thanks for sharing the shining days during these years. And, most importantly, thanks to my parents. Thanks for the unconditional love and support.

I had a very long acknowledgment in my bachelor thesis, which summarized my feelings about my past life, my thoughts on my future life, and my attitude toward science research during that time. However, when writing this acknowledgment, I don't know where to start. Thinking about the reason, I think that for the first year of my master, I had a good time. Not only because I picked up the life of listening to lectures and taking exams, which makes me feel more like a student, neither only because I traveled to lots of places within or outside of the Netherlands. The most important reason is that I regarded it as nothing but my first year of master study. I had a pure aim and was able to enjoy my life. However, for the second year, I may regarded it more as the transition between the bachelor and PhD rather than the second year of my master. I considered too much about my future, trapped in it, became indecisive, couldn't feel I was living in the "current", and gave myself too much pressure. However, this is inevitable. Every time there is a change in my life, I can't help to be trapped in it. It's just because the master study only has two years, thus the part of the hard time during the "change" takes more proportion. Therefore, I hope in the future, I can have the chance to slow down. Don't always focus on "the next step" and "the things I have to achieve before xxx". When the way is blocked and you cannot step forward, then just stop and have a rest.

Although I said I don't have too many things to say, when I write here, there are already many words. Because it's my master thesis, which will be recorded in the university database forever (compared with my life). Although nobody cares what you write, I always want to use it to record some of my thoughts on my master life and my current thoughts toward science research, which once I thought was important for my life but now become more and more ambiguous for me because I think it may be not written on my destiny. Just like writing something on the end of an ancient book, put it on a shelf in the deep corner of the library and lock the door. Using this way, to say goodbye to my two-year life, to thank the people who accompany me in this two-year journey, and to say goodbye to all of you. Thanks a lot.

A

ADDITIONAL INFORMATION

A.1. BOUNDARY CONDITIONS FOR UNIT CELL SIMULATION

The detailed way of setting the boundary conditions for the unit cell simulation is introduced in this section.

For the symmetry plane in the x-y plane, the perfect magnetic conductor (PMC) condition is applied. This boundary condition guarantees that only the modes whose magnetic fields are perpendicular to this plane can be supplied in the structure, which is a necessary condition for the TE mode. In addition, as the PMC doesn't allow the tangential component of the magnetic field to exist within the plane, the unwanted electric field along the z direction is eliminated. As for the symmetry plane in the z-x plane, the perfect electric conductor (PEC) condition is applied. Similarly, this boundary condition only supports the mode with the electric field perpendicular to this surface, e.g. along the y-axis, and eliminates ones that have tangential components. In addition, the symmetry conditions are also met with these boundaries because of the mathematical property of the wave function (the first-order spacial derivation should be 0 at the symmetry point).

A.2. FABRICATION PROCEDURE

In this section, we introduce the fabrication procedure to get the devices in detail.

We start with the commercial silicon wafer as the substrate of our devices. After that, high-stress silicon nitride is grown on the silicon wafer with a thickness of 300 nm by LPCVD. Then by spin coating, the resist (CSAR62) is coated on the top of the silicon nitride. Then we bake it for 3 minutes to let the resist to be formed. The pattern based on our device is written on the resist by the e-beam lithography. After this, in the development step, the e-beam-exposed areas on the resist are removed. Then we conduct dry etching and the areas of the silicon nitride that are not covered by the resist will be etched. As the pattern is already patterned on the resist, through dry etching, we can transfer the pattern to the silicon nitride. After we etch through the silicon nitride, we clean all the resist by hot DMF (Dimethylformamide). Finally, we conduct dry release using SF6 and O2, which only react with silicon and won't influence the silicon nitride. In this way, we etch the area under our devices and suspend them, which allows us to deform them in our experiment. The sketch of the whole fabrication procedure is shown in Fig. A.1.

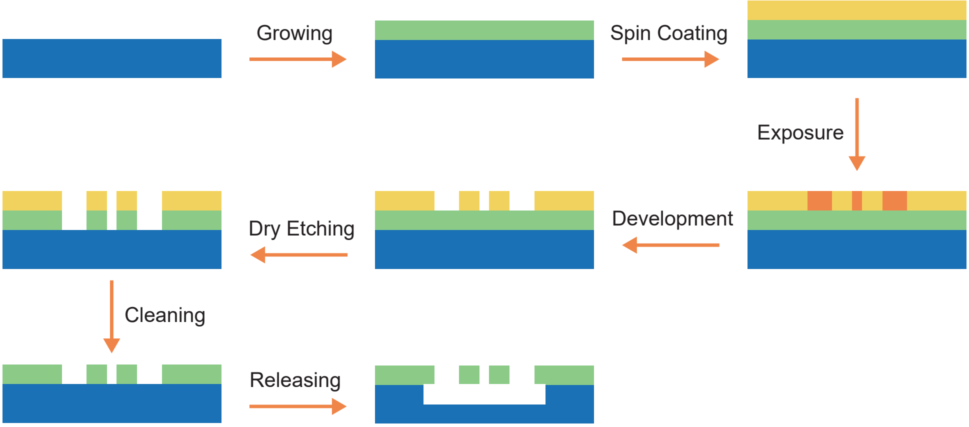

Figure A.1: The fabrication procedure through we fabricate our device. The blue layer refers to the silicon. The green layer refers to the silicon nitride. The yellow layer refers to the resist.

B

REFERENCE

REFERENCES

[1] Helge Aasen, Eija Honkavaara, Arko Lucieer, and Pablo J Zarco-Tejada. Quantitative remote sensing at ultra-high resolution with uav spectroscopy: a review of sensor technology, measurement procedures, and data correction workflows. *Remote Sensing*, 10(7):1091, 2018.

[2] Immo Appenzeller. *Introduction to astronomical spectroscopy*, volume 9. Cambridge University Press, 2012.

[3] Neil W Ashcroft and N'David Mermin. Solid state physic holt. *Rinehart and Winston, New York, USA*, 1976.

[4] Markus Aspelmeyer, Tobias J Kippenberg, and Florian Marquardt. Cavity optomechanics. *Reviews of Modern Physics*, 86(4):1391, 2014.

[5] Ali Can Atik, Metin Dündar Özkan, Ebru Özgür, Haluk Külah, and Ender Yıldırım. Modeling and fabrication of electrostatically actuated diaphragms for on-chip valving of mems-compatible microfluidic systems. *Journal of Micromechanics and Microengineering*, 30(11):115001, 2020.

[6] Christina P Bacon, Yvette Mattley, and Ronald DeFrece. Miniature spectroscopic instrumentation: applications to biology and chemistry. *Review of Scientific instruments*, 75(1):1–16, 2004.

[7] Paul E Barclay, Kartik Srinivasan, Matthew Borselli, and Oskar Painter. Experimental demonstration of evanescent coupling from optical fibre tapers to photonic crystal waveguides. *Electron. Lett*, 39(11):842–844, 2003.

[8] Jasper Chan. *Laser cooling of an optomechanical crystal resonator to its quantum ground state of motion*. California Institute of Technology, 2012.

[9] Jasper Chan, Matt Eichenfield, Ryan Camacho, and Oskar Painter. Optical and mechanical design of a “zipper” photonic crystal optomechanical cavity. *Optics Express*, 17(5):3802–3817, 2009.

[10] Jasper Chan, Amir H. Safavi-Naeini, Jeff T. Hill, Seán Meenehan, and Oskar Painter. Optimized optomechanical crystal cavity with acoustic radiation shield. *Applied Physics Letters*, 101(8):081115, 08 2012.

[11] Risheng Cheng, Chang-Ling Zou, Xiang Guo, Sihao Wang, Xu Han, and Hong X Tang. Broadband on-chip single-photon spectrometer. *Nature communications*, 10(1):4104, 2019.

[12] Parag B Deotare, Irfan Bulu, Ian W Frank, Qimin Quan, Yinan Zhang, Rob Ilic, and Marko Loncar. All optical reconfiguration of optomechanical filters. *Nature Communications*, 3(1):846, 2012.

[13] Parag B Deotare, Murray W McCutcheon, Ian W Frank, Mughees Khan, and Marko Lončar. Coupled photonic crystal nanobeam cavities. *Applied Physics Letters*, 95(3), 2009.

[14] Perry Edwards, Chenji Zhang, Baigang Zhang, Xiangqian Hong, Vivek K Nagarajan, Bing Yu, and Zhiwen Liu. Smartphone based optical spectrometer for diffusive reflectance spectroscopic measurement of hemoglobin. *Scientific reports*, 7(1):12224, 2017.

[15] Matt Eichenfield, Ryan Camacho, Jasper Chan, Kerry J Vahala, and Oskar Painter. A picogram-and nanometre-scale photonic-crystal optomechanical cavity. *nature*, 459(7246):550–555, 2009.

[16] Time-Harmonic Electromagnetic Fields. *Time harmonic electromagnetic fields*. McGraw-Hill, 1961.

[17] CM Gärtner. *Advanced membrane architectures for multimode optomechanics*. PhD thesis, TUD, 2020.

[18] Teodoro Graziosi. Design of a tunable optomechanical cavity, 2015.

[19] David J Griffiths. *Introduction to electrodynamics*. Cambridge University Press, 2023.

[20] David J Griffiths and Darrell F Schroeter. *Introduction to quantum mechanics*. Cambridge university press, 2018.

[21] Wladick Hartmann, Paris Varytis, Helge Gehring, Nicolai Walter, Fabian Beutel, Kurt Busch, and Wolfram Pernice. Broadband spectrometer with single-photon sensitivity exploiting tailored disorder. *Nano letters*, 20(4):2625–2631, 2020.

[22] Bas Hensen. *Quantum nonlocality with spins in diamond*. PhD thesis, TUD, 2016.

[23] John D Joannopoulos, Steven G Johnson, Joshua N Winn, and Robert D Meade. Molding the flow of light. *Princet. Univ. Press. Princeton, NJ [ua]*, 2008.

[24] Steven G Johnson, Mihai Ibanescu, MA Skorobogatiy, Ori Weisberg, JD Joannopoulos, and Yoel Fink. Perturbation theory for maxwell's equations with shifting material boundaries. *Physical review E*, 65(6):066611, 2002.

[25] Steven G Johnson and John D Joannopoulos. Block-iterative frequency-domain methods for maxwell's equations in a planewave basis. *Optics express*, 8(3):173–190, 2001.

[26] Charles Kittel and Paul McEuen. *Introduction to solid state physics*. John Wiley & Sons, 2018.

[27] Ang Li and Yeshaiahu Fainman. On-chip spectrometers using stratified waveguide filters. *Nature communications*, 12(1):2704, 2021.

[28] Zin Lin, Thomas Alcorn, Marko Loncar, Steven G Johnson, and Alejandro W Rodriguez. High-efficiency degenerate four-wave mixing in triply resonant nanobeam cavities. *Physical Review A*, 89(5):053839, 2014.

[29] Martin Maldovan and Edwin L Thomas. Diamond-structured photonic crystals. *Nature materials*, 3(9):593–600, 2004.

[30] Andrew JS McGonigle, Thomas C Wilkes, Tom D Pering, Jon R Willmott, Joseph M Cook, Forrest M Mims III, and Alfio V Parisi. Smartphone spectrometers. *Sensors*, 18(1):223, 2018.

[31] Robert D Meade, AM Rappe, KD Brommer, JD Joannopoulos, and OL Alerhand. Accurate theoretical analysis of photonic band-gap materials. *Physical Review B*, 48(11):8434, 1993.

[32] Babak Momeni, Ehsan Shah Hosseini, Murtaza Askari, Mohammad Soltani, and Ali Adibi. Integrated photonic crystal spectrometers for sensing applications. *Optics communications*, 282(15):3168–3171, 2009.

[33] Rajesh V Nair and Ramarao Vijaya. Photonic crystal sensors: An overview. *Progress in Quantum Electronics*, 34(3):89–134, 2010.

[34] Raviv Perahia, JD Cohen, Sean Meenehan, TP Alegre, and Oskar Painter. Electrostatically tunable optomechanical "zipper" cavity laser. *Applied Physics Letters*, 97(19), 2010.

[35] Miloš A Popović, Christina Manolatou, and Michael R Watts. Coupling-induced resonance frequency shifts in coupled dielectric multi-cavity filters. *Optics express*, 14(3):1208–1222, 2006.

[36] Michael JD Powell. On search directions for minimization algorithms. *Mathematical programming*, 4:193–201, 1973.

[37] Tomohiro Tetsumoto and Takasumi Tanabe. High-q silica zipper cavity for optical radiation pressure driven moms switch. *AIP Advances*, 4(7), 2014.

[38] Andreas Tittl, Aleksandrs Leitis, Mingkai Liu, Filiz Yesilkoy, Duk-Yong Choi, Dragomir N Neshev, Yuri S Kivshar, and Hatice Altug. Imaging-based molecular barcoding with pixelated dielectric metasurfaces. *Science*, 360(6393):1105–1109, 2018.

[39] Md Gius Uddin, Susobhan Das, Abde Mayeen Shafi, Lei Wang, Xiaoqi Cui, Fedor Nigmatulin, Faisal Ahmed, Andreas C Liapis, Weiwei Cai, Zongyin Yang, et al. Broadband miniaturized spectrometers with a van der waals tunnel diode. *Nature Communications*, 15(1):571, 2024.

[40] Zhu Wang, Soongyu Yi, Ang Chen, Ming Zhou, Ting Shan Luk, Anthony James, John Nogan, Willard Ross, Graham Joe, Alireza Shahsafi, et al. Single-shot on-chip spectral sensors based on photonic crystal slabs. *Nature communications*, 10(1):1020, 2019.

[41] Martin A Wolff, Simon Vogel, Lukas Splitthoff, and Carsten Schuck. Superconducting nanowire single-photon detectors integrated with tantalum pentoxide waveguides. *Scientific Reports*, 10(1):17170, 2020.

[42] Zongyin Yang, Tom Albrow-Owen, Weiwei Cai, and Tawfique Hasan. Miniaturization of optical spectrometers. *Science*, 371(6528):eabe0722, 2021.

[43] Pochi Yeh and Michael Hendry. Optical waves in layered media. *Physics Today*, 43(1):77, 1990.

[44] Hoon Hahn Yoon, Henry A Fernandez, Fedor Nigmatulin, Weiwei Cai, Zongyin Yang, Hanxiao Cui, Faisal Ahmed, Xiaoqi Cui, Md Gius Uddin, Ethan D Minot, et al. Miniaturized spectrometers with a tunable van der waals junction. *Science*, 378(6617):296–299, 2022.

[45] Senlin Zhang, Zhengdong Yong, Yuguang Zhang, and Sailing He. Parity-time symmetry breaking in coupled nanobeam cavities. *Scientific Reports*, 6(1):24487, 2016.